

Award Accounts

The Chemical Society of Japan Award for Creative Work for 2004

Theoretical Studies on the Structure and Dynamics of Water, Ice, and Clathrate Hydrate

Hideki Tanaka* **and Kenichiro Koga**

Department of Chemistry, Faculty of Science, Okayama University, 3-1-1 Tsushima, Okayama 700-8530

Received March 28, 2006; E-mail: htanakaa@cc.okayama-u.ac.jp

We have investigated various anomalous properties of water such as the divergent character of the thermodynamic functions and liquid–liquid transition in supercooled water, the phase behaviors of water and new ices in nanoscale confinement, the thermodynamic stability of clathrate hydrates over a wide range of pressure, and anomalous thermodynamic and structural properties of ices. These are studied by some theoretical calculations and Monte Carlo/molecular dynamics computer simulations. It is demonstrated that the potential energy surface and the connectivity of supercooled water are keys to understand why liquid–liquid transition can take place in deeply supercooled water. A tetrahedral coordination of water is preserved even in extreme confinements, forming tubule ice and bilayer crystalline (or amorphous) ice, although the heavy stress makes the bond angles and lengths different from the ideal values. Thermodynamic stability of clathrate hydrates, including double occupancy, is more accurately predicted by considering the host–guest coupling and other factors. The negative thermal expansivity and the change in slope of the Debye–Waller factor of ice are explained with a simple model of water.

1. Introduction

It has long been recognized that liquid water does not share many physical properties with ordinary liquids or what we call simple liquids, such as a density maximum at 4 °C, a large heat capacity, and a decrease in viscosity with increasing pressure.[1,2] Much effort has been devoted to accounting for those unique quantities of this ubiquitous substance on the earth. In doing this, use has been invariably made of hydrogen bonds on which various models are based; most water molecules are connected by hydrogen bonds in ambient temperature and pressure ranges. However, our conceptual ideas on water structure (mixture and continuum model) have not yet been tested thoroughly against laboratory experiments and thus, have been nothing more than speculative ones.[2,3] Development of computer simulation techniques, such as molecular dynamics (MD) and Monte Carlo (MC), enables us to establish a bridge between macroscopic observables and the microscopic structure on the nano scale over the last three decades.[4] These methods can be used to study physicochemical properties of liquid water, ices, and clathrate hydrates from a microscopic viewpoint. We will address, in this account, (1) microscopic view of polyamorphism in supercooled water in terms of liquid–liquid transition associated with a change in potential energy surface, (2) phase behaviors of water and new ice forms in quasi-one and two-dimensional space, (3) thermodynamic stability of clathrate hydrates beyond empirical treatments, and (4) physical origins of some of the anomalies of ices at atmospheric pressure. These issues are studied by some theoretical calculations including MD and MC simulations.

2. Intermolecular Interactions, MD Simulations, and Inherent Structures

In computer simulations, intermolecular interactions for water molecules are, of course, a crucial factor, upon which the reliability of the analysis rests. Although there is no apriori reason to neglect intramolecular vibrational motions, most of the proposed potential functions for water are rigid rotors having several interaction sites. Use of a central force model, which makes no distinction between intra and intermolecular interactions, is inevitable in case that a main aim of the simulation is to elucidate the coupling between intra and intermolecular motions. However, central force models are still primitive compared to rigid rotor models, despite their apparent importance, mainly because it is difficult to describe both intra and intermolecular interactions with a common functional form. Therefore, we will focus on only rigid rotor models in the following study.

The potential energy of an assembly of N water molecules, Φ_N, in the absence of external field is formally described as

$$\Phi_N = \sum_{i<j} \phi_2(\mathbf{r}_i, \mathbf{r}_j) + \sum_{i<j<k} \phi_3(\mathbf{r}_i, \mathbf{r}_j, \mathbf{r}_k) + \ldots, \quad (1)$$

where ϕ_2 is a dimerization energy and ϕ_3 is three body interaction, which cannot be described by the sum of the dimerization energy. Each potential term depends on both the center of

Published on the web November 9, 2006; doi:10.1246/bcsj.79.1621

mass positions and orientations abbreviated by **r**. It is generally believed that higher body interactions other than two body interaction are about 20% of the total energy, and therefore, it affects significantly the thermodynamic properties of water, especially when spatial density fluctuations are large.[3]

Nonempirical potential models are mostly designed to include only a two body interaction. Empirical potential functions include higher body interactions effectively in somewhat averaged manner. Some potential functions, called poralizable models, can take an induced dipole interaction into account. In general, empirical potentials seem to be superior for reproducing thermodynamic properties of pure water. Most of the pair potentials for water dimer comprise point charges which mimic hydrogen bonds in a small separation and electrostatic multipole interactions in a long distance region. There are usually three point charges, as in the TIP4P potential.[5] Four-point charge models are known to overemphasize a tetrahedral feature of structure in liquid state.[6,7]

In MD simulations of bulk water, a periodic boundary condition is applied to all three directions. If water is confined, it is applied only to the directions free from the confinement. MD simulations are usually performed with a fixed temperature and pressure using Nosé-Andersen's constant temperature–pressure method.[8,9] For quasi-one- and two-dimensional water, the internal axial (normal) pressure p_{zz} (the pressure tensor parallel to the axis or normal to the planes) or the lateral pressure p_{xx} and p_{yy} is kept constant using a modified Andersen's method.[10]

The configurations generated from MD (or MC) simulation are called instantaneous (I-) structures. The minimum energy quenched (Q-) structures correspond to stable points in configuration space. Therefore, the potential energy for the I-structures is composed of two contributions: (1) the potential energy of the Q-structures and (2) upward shifts from the Q-structures due to thermal energy.[11,12] The steepest descent minimization is applied to obtain Q-structures from the I-structures.

3. Supercooled Water and Polyamorphism

Supercooled water and amorphous ice intrigue us in their unique phase behavior: A high density amorphous ice undergoes a low density amorphous (HDA-LDA) solid-to-solid phase transition below 140 K, which was discovered by Mishima and co-workers.[13,14] It is referred to as polyamorphism. Later, a high-density liquid to low-density liquid (HDL-LDL) phase transition was reported based on computer simulations of supercooled water.[15–21] However, such a liquid–liquid transition has not been observed in a laboratory experiment because it is located in the deeply supercooled region. It was suggested that the transition is responsible for various anomalies in water by both statistical mechanical calculations with simple models and MD/MC simulations in which a nucleation is suppressed in a short period. The anomalies are so enhanced in supercooled region that the heat capacity and the isothermal compressibility have divergent characters centered at 228 K.[22,23] Thus, it was tempted to account for the anomalies in water in terms of the (hidden) phase transition and its terminal point (a second critical point), the latter of which can be associated with the large fluctuations in the corresponding thermodynamic properties. In fact, a transition-like behavior was observed in computer simulation study although the exact phase boundary has not been established. Its location is also dependent on the water–water interaction model adopted. Furthermore, a fragile-to-strong liquid transition was proposed in supercooled water near 228 K,[24,25] which was also observed in deeply supercooled water confined in hydrophilic pores.[26,27] The LDA-HDA transition might be structurally analogous to low- and high-pressure ice polymorphs. Recent studies suggest existence of another amorph, called VHDA (very high-density amorphous), in addition to LDA and HDA.[28,29] Theoretical studies on these amorphs have been limited, and it is still controversial as to whether or not VHDA is a different phase from HDA and whether LDA is a different phase from HDA.[30–34]

In order to examine the difference in structure between LDA(L) and HDA(L), a series of MD simulations are performed for the number of molecules $N = 216$, and the temperatures, T, of 298, 273, 253, 233, 223, 213, 203, 193, 183, and 173 K.[35] It is evident from Fig. 1 that the potential energy in I-structure drops abruptly around 210 K. Although the break may not be identified definitely with a liquid–liquid phase transition, it is deduced reasonably that this is associated with such a transition or the second critical point at which the LHD-HDL phase boundary terminates.[15,17,18,36] The potential energy of the Q-structure depends significantly on temperature between 298 and 220 K. This temperature dependence suggests that water above 220 K is a fragile liquid. Below 200 K, the slope of the curve is negligibly small, and the potential energy of the Q-structure is almost constant followed by a sudden drop around 210 K. The change in the temperature dependence of potential energy can be associated with a potential energy surface on which the trajectory moves around in the configuration space. The mean square displacement, $\langle[\mathbf{R}_i(t) - \mathbf{R}_i(0)]^2\rangle$, concerning the motion of individual water molecules is calculated, where $\mathbf{R}_i(t)$ is a position of i-th molecule at time t and the aver-

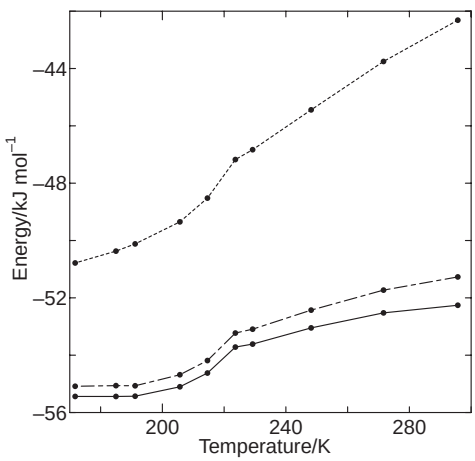

Fig. 1. Potential energies of I- (dotted line), Q- (solid line), and intermediated (dash-dot line) structures versus temperature. Individual points are the potential energies in kJ mol^{-1} averaged over 500 configurations generated by NEV (microcanonical) MD simulations. The densities determined by NPT (isothermal–isobaric) simulations at 0.1 MPa are fixed to constant values in NEV MD simulations.

age is denoted by angular bracket. It is linear with time t even at 190 K (not shown here), suggesting that water at this temperature is still liquid.[18] Thus, water below 210 K is a rather strong liquid, which has a simple potential surface described by the Arrhenius-type excitation. The thermal energy $(E_I - E_Q)$ is large at higher temperature but becomes smaller below 210 K (see Fig. 1). Since the thermal energy (per mole) corresponding to harmonic oscillators is $3N_A k_B T$, where N_A and k_B are the Avogadro's number and Boltzmann constant, respectively, the large change in the thermal energy is associated solely with the change of the anharmonic energy around 210 K. However, the anharmonic energy below 210 K is still large while the diffusion is normal. In the cases of a Lennard–Jones (LJ) mixture and silica,[37–39] the anharmonic energy becomes negligibly small at low temperature once the Q-structure energy drops upon cooling. Thus, the temperature in such systems is associated with the glass transition, and the systems are considered to be arrested mostly inside potential basins with occasional jump-like motions. This is in contrast to supercooled water: Diffusive motions prevail,[40–42] and the anharmonic character remains even around 190 K. In water, the potential energy for the Q-structures decreases by more than 2.3% from 298 to 220 K. Then, a more abrupt drop in Q-structure energy (2.5%) is observed in the narrow temperature range between 220 and 200 K (Fig. 1). This feature is different from the cases of silica and LJ mixture. This suggests that there could be a fragile–strong transition which occurs not by dynamically arrested kinetics but by a potential energy surface change.

One of the most important issues on polyamorphism is to address why two phases exist in one component liquid state. We may also ask what is the most noticeable difference in structure between LDA and HDA. We show structural difference between two liquid states is accounted for in terms of the fluctuation of local order and the network pattern among the ordered water molecules.[43] The number of water molecules hydrogen-bonded with four neighbors increases drastically upon the transition from HDA to LDA for any reasonable choice of hydrogen-bond criteria.[18] The local order of LDA should be much enhanced compared with HDA. Thus, a perfect tetrahedral coordination is a key to local ordering. The coordination number can be defined reasonably by the number of other molecules (oxygen atoms) within the first minimum distance of the corresponding radial distribution function, $g(r)$. The running coordination number, $n(r)$, is given as

$$n(r) = \rho \int_0^r g(r')\mathrm{d}\mathbf{r}', \tag{2}$$

where r is the molecular separation and ρ stands for the number density. The experimental coordination number at room temperature is 4.4 according to the above definition with a molecular separation, r_m, at which $g(r)$ takes the first minimum.[1] This value is not expected to change significantly upon temperature decrease from 233 K (HDL) to 193 K (LDL). However, a difference appears in its fluctuation, and the number of species-4 decreases with increasing temperature (species-j is a water molecule to which other j molecules are coordinated). A difference in coordination number fluctuation and its spatial correlation are examined to show that the phase transition is

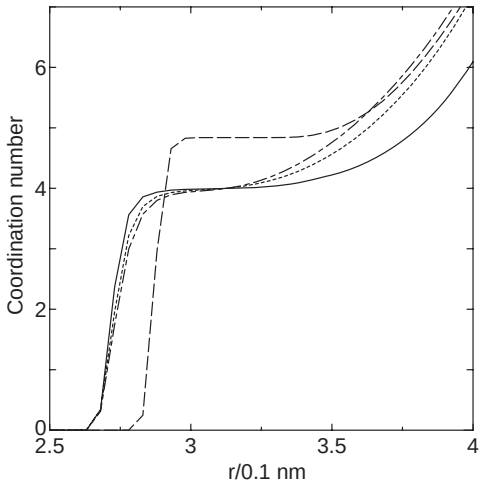

Fig. 2. Running coordination number in Q-structure as a function of distance from a central molecule at the origin for water and HS model, which was invented to mimic one-dimensional water structure. Solid line; water at 193 K (LDL), dotted line; water at 233 K (HDL), and dash-dot line at 298 K (HDL), dashed line; HS model at 298 K.

associated with a percolation transition of locally ordered clusters.[44] To show importance of this property, also performed is an MD simulation for a model which has a single interaction site yet has a similar $g(r)$ to water (HS model).[45] The coordination numbers of water at three temperatures are all reduced to approximately 4.0 as shown in Fig. 2: The local structure (within $r_m = 0.3$ nm), after removing the thermal energy, remains unchanged on average in liquid water. This does not mean all of the water molecules participate in the ice-like structure. The percentages of various species are given in Table 1. Species-4 is the most dominant one even in HDL. In water, its population increases drastically upon transformation from HDL to LDL. Although the number of each species is sensitive to temperature, their mean values, approximately 4, at all three temperatures are rather insensitive. Even though the coordination number (also $g(r)$) for the HS model in I-structure is close to that of water, it is fairly different in Q-structure from that of water and exhibits a wide distribution with several kinds of species (species-j, $j = 1$ to 8).

A new quantity, fluctuation of the coordination number, is defined by

$$\Delta n(r) = \langle [N_i(r) - n(r)]^2 \rangle^{1/2}, \tag{3}$$

where $N_i(r)$ is the coordination number for i-th molecule at an given instant and $\langle\ \rangle$ stands for average taken over all molecules and generated configurations. The fluctuations of coordination number are shown in Fig. 3. The fluctuation, $\Delta n(r)$, reaches its minimum value around the first minimum of $g(r)$. If molecules are randomly distributed on a body-centered cubic lattice and half the sites are occupied, its fluctuation is large ($\Delta n(r_m) = 2^{1/2}$). In water, the fluctuation is 0.45 for HDL while 0.25 for LDL. The number of defects (molecules other than species-4) are small in real water at ambient temperature than in a randomly occupied case, and the transformation to LDL gives rise to further reduction of defects. A question is raised as to how those defects are spatially correlated with

Table 1. Coordination Number Distribution p_i (%) Having i Neighbors and Probability Distribution g_{ij} (%) for a Molecule Next to a Central One Having j Neighbor Molecules Conditional on that the Central Molecule Has i Neighbors at Temperature T(K) and 0.1 MPa[a)]

p_i $T\backslash i$	2	3	4	5	6
298 water	1	18	74	7	0
233 water	1	11	83	5	0
193 water	0	3	95	2	0
298 HS	7	21	35	25	8
g_{ij} $i\backslash j$	3	4	5		
water $T = 298$					
3	10	75	14		
4	14	77	8		
5	22	73	4		
water $T = 233$					
3	4	80	15		
4	7	86	7		
5	15	82	3		
water $T = 193$					
3	1	87	11		
4	2	96	2		
5	11	89	0		
HS $T = 298$					
3	18	37	30		
4	17	36	31		
5	16	34	32		

a) The cut-off length for coordination number is 0.3 nm.

each other. We define a probability distribution g_{ij} for a molecule next to a central one having j neighbor molecules conditional on that the central molecule has i neighbors. The probability is also given in Table 1. Clearly, defects are correlated such that molecules of species-3 repel each other (so do species-5 molecules) while a species-3 attracts a species-5.

It has been recognized that water at ambient temperature is a transient gel and that hydrogen bonds form an infinite size of cluster.[44] Even when we consider a site-percolation of only species-4 water at room temperature, water is percolated as is clear from Table 1. The site percolation threshold for those systems is as low as that of diamond structure 0.4,[46] which should be compared with $p_4 = 0.74$ for water. This suggests that a larger correlation unit of species-4 should be considered in order to distinguish LDL from HDL. Thus, we impose a further condition; i.e., a central species-4 has 4 neighboring species-4. This procedure is repeated up to the third neighbors, and ratios of the perfectly coordinated water molecules are given in Table 2. There is a large difference between two liquid phases for a spatial correlation up to the second neighbors. Since we consider site-percolation, the percolation threshold p_s is related empirically to the packing fraction, η as

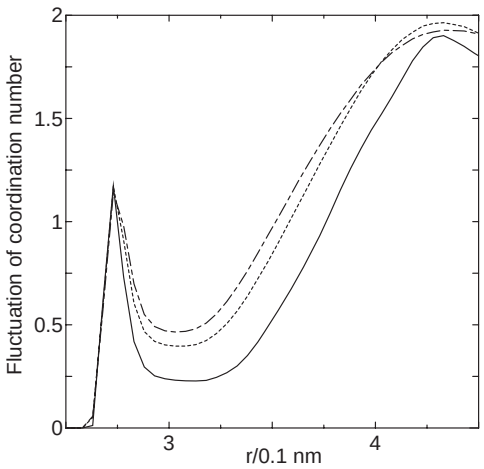

Fig. 3. Fluctuation of the running coordination number. Solid line; water at 193 K (LDL), dotted line; water at 233 K (HDL), and dash-dot line; water at 298 K (HDL).

Table 2. Probability (%) of Water Molecules which Have Only Species-4 up to i-th Neighbors[a)]

$T\backslash i$	0	1	2	3
298	74	26 (30)	1 (1)	0
233	83	44 (47)	8 (6)	0
193	95	80 (81)	50 (46)	20

a) The probability of random distribution of species-4 is given in parenthesis.

$$p_s\eta \simeq 0.16, \tag{4}$$

for three-dimensional system.[47] The packing fraction is calculated by

$$\eta = \pi\rho r_m^3/6. \tag{5}$$

Hence, the threshold value p_s is approximately 0.34 (similar to the diamond structure), which implies that water at 193 K is percolated while water at 233 K or higher is not.

Another interesting feature is how a potential energy surface visited by a system is altered upon transition from HDA to LDA (HDL-LDL). The potential landscape has been related to not only thermodynamic but dynamic properties.[48,49] In particular, it was discussed in conjunction with the strong–fragile characters of network forming substances such as water, silica, silicon, etc.[49,50] The potential surface is described by two components: (1) the intrabasin structures associated with vibrational motions and (2) the distribution of the potential minimum (Q-) structures in configuration space, which is equivalent to the configurational entropy. The number of the distinct energy minima was enumerated by separate evaluation of various free energy components.[51] We provide complementary information on the interbasin structures in the potential surface of the supercooled water; how other basins are distributed in the vicinity of the basin along the MD trajectory. The intrabasin structures have been investigated for simple liquid mixtures and silica.[37,38] It was shown for LJ mixtures that the structure and dynamics of low temperature supercooled state are dominated by the potential landscape, whereas the dynamics at high

temperature is dominated by the simple kinetic process, that is, the activation is the Arrhenius type. Although the Arrhenius type may be apparently recovered in deeply supercooled state, the potential surface is rugged, and the dynamics on it seems to be complicated.[37] Here, examined are the intrabasin structures, paths from the I-structures to the corresponding Q-structures at several state points where various thermodynamic properties differ significantly.[17,18]

The mass-weighted distance in configuration space for polyatomic systems seems to be a useful quantity.[38] The distance between two points in configuration space is defined as

$$\Delta R = \left(\frac{\sum_i m_i (\mathbf{s}_i - \mathbf{s}'_i)^2}{\sum_i m_i} \right)^{\frac{1}{2}}, \tag{6}$$

where m_i and $\mathbf{s}_i$ stand for the mass and the (three-dimensional) coordinate of i-th atom for the intermediate point along the steepest descent path and $\mathbf{s}'_i$ indicates the coordinate of i-th atom in either I- or Q-structure, respectively. This quantity is equivalent to the distance between the mass-weighted coordinates in configuration space defined as

$$\Delta R = |\mathbf{R} - \mathbf{R}'|, \tag{7}$$

where $\mathbf{R}^t = (m_1^{1/2}\mathbf{s}_1^t, m_2^{1/2}\mathbf{s}_2^t, \ldots, m_{3N}^{1/2}\mathbf{s}_{3N}^t)/(\sum_i m_i)^{1/2}$. In the following study, we call ΔR defined above a distance in configuration space, and $\mathbf{R}_\mathrm{I}$ and $\mathbf{R}_\mathrm{Q}$ stand for $\mathbf{R}'$ at I- and Q-structure, respectively.

We examine three sorts of Q-structures obtained from the MD simulations at $T = 193$, 233, and 298 K and the subsequent quenching. The potential energy surfaces for liquid water in the vicinity of the basin that the MD trajectory explores are investigated by exciting a system and quenching it. The excitation is made by translating and rotating water molecules whose magnitude is measured by the normal mode energy. The present method aims at moving molecules by normal mode excitation since the normal mode coordinates provide mutually orthogonal directions, and the potential energy curvatures are characterized by the normal mode frequencies in the immediate vicinity of a given basin center. The potential surface in the vicinity of the configuration that the system visits was examined previously by the normal mode excitation (the system was excited by rendering kinetic energy instead of the potential energy)[4,52] and in conjunction with the number of imaginary modes.[53] Here, the interbasin structures are explored by encompassing the sampling region that contains thousands of other potential basins. The original Q-structures at each temperature are denoted by $\mathbf{r}_0$, which includes all the coordinates of water molecules ($6N$-dimensional vector of individual molecular center of mass coordinates and Euler angles) for a given system. Then, molecules are moved by $\Delta\mathbf{r}_e$, which is calculated from

$$\Delta\mathbf{r}_e = \mathbf{m}^{-1/2}\mathbf{U}^\dagger\mathbf{q}, \tag{8}$$

where $\mathbf{U}$, $\mathbf{m}$, and $\mathbf{q}$ are the unitary matrix to diagonalize the corresponding Hessian matrix, the mass matrix, and a set of normal coordinates, respectively. The system is excited by giving a set of normal mode amplitudes. The total mode energy is given by

$$E_\mathrm{mode} = \frac{1}{2}\sum_{i=1}^{6N-3}(\omega_i q_i)^2, \tag{9}$$

where ω_i is the angular frequency of the i-th mode. Since $\langle q_l q_m \rangle = 0$ for $l \neq m$, the thermal average of the mean square displacement of i-th element of $\Delta\mathbf{r}_e$ for a harmonic system is given by

$$\langle \Delta r_e^{(i)2} \rangle = \sum_{j,k,l} s_{ij} s_{ik} u_{jl} u_{kl} \langle q_l^2 \rangle, \tag{10}$$

where ij-elements of $\mathbf{m}^{-1/2}$ and $\mathbf{U}^\dagger$ are denoted by s_{ij} and u_{ij}. In the case of classical mechanics, $\langle q_l^2 \rangle$ is given simply by

$$\langle q_l^2 \rangle = k_\mathrm{B}T/\omega_l^2. \tag{11}$$

It is assumed that all the modes have the same potential energy $k_\mathrm{B}T/2$ upon the excitation. Thus, we can determine all of the molecular displacements ($\Delta\mathbf{r}_e$) due to the normal mode excitation except for the sign of each element. In the following arguments on the distances in configuration space, the molecular coordinates (displacements) denoted by $\mathbf{r}$ ($\Delta\mathbf{r}$) are converted to the mass-weighted atomic coordinates (displacements) denoted by $\mathbf{R}$ ($\Delta\mathbf{R}$) similar to the analysis of the intrabasin structures.

The average distance between I- and Q-structures defined by Eq. 7 (root-mean-square displacement (RMSD)) is a measure of the amplitude arising from sum of the harmonic and anharmonic vibrations. Since one of the key parameters to characterize the potential basin structures is the magnitude of the anharmonicity of the vibrational motions in individual potential basins, it is desirable to evaluate the displacements originated from the harmonic motions separately. To do this, also calculated is the RMSD arising from the harmonic vibrations. The RMSDs of individual atoms from the harmonic vibrations can be obtained via the normal mode amplitudes. Since the displacement from the Q-structure, $\Delta\mathbf{r}_e$, in configuration space is related to the normal mode coordinate $\mathbf{q}$ as given in Eq. 8, the mean square amplitudes are again given by Eqs. 10 and 11 at a given temperature although the harmonic $|\Delta\mathbf{r}_e|$ inside a potential basin is much smaller than that in normal mode excitation for examining interbasin structure. Since Eq. 10 gives the mean square displacements of the center of mass coordinates and Euler angles separately, these are transformed into the atomic displacements, ΔR, assuming the orientational displacements are small. Hence, we compare the RMSD of the real system with that of the corresponding harmonic one.

The RMSD for water is plotted in Fig. 4 together with that corresponding harmonic system. The temperature dependence of RMSD changes around 210 K. On the other hand, the RMSD for harmonic system is almost linear irrespective of the fact that the vibrational density of state depends weakly on temperature.[18] Note that there is a fairly large difference between real and harmonic systems even below 210 K. In other words, the break in the RMSD plot does not arise from a phenomenon associated with a glass transition. This interpretation is consistent with the fact that the experimentally observed glass-transition temperature is low, around 136 K,[40–42] and a view that deeply supercooled water undergoes a fragile–strong transition.[25] It should also be noted that the relative magnitude

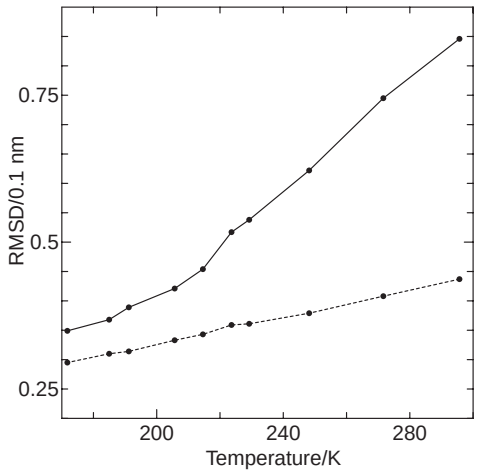

Fig. 4. Root-mean-square displacements from the centers of basins by MD simulation (solid line) together with those of the harmonic oscillators (dotted line).

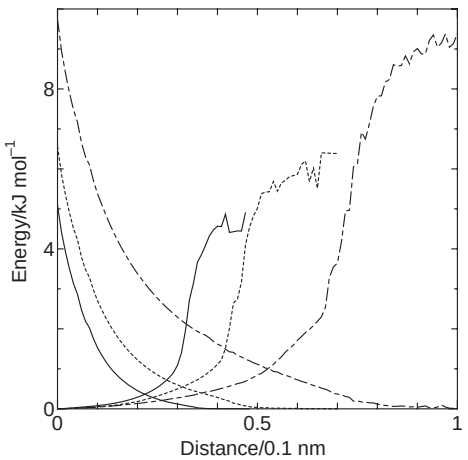

Fig. 5. The average of the potential energy curves both from the I-structures and from the Q-structures. Temperatures are 193 K (solid line), 233 K (dotted line), and 298 K (dash-dot line).

of the anharmonic contribution to the RMSD in water at 193 K is approximately twice as large as that of silica near the glass-transition temperature.

The one-dimensional potential energy surface along the steepest descent paths averaged over 500 configurations are plotted in Fig. 5 against the distance from either the I- or Q-structure. In case of all the downward curves, the slope gradually decreases and finally arrives at an asymptotic value. On the other hand, the curves become suddenly steeper in distant region in upward curve. Since the thermal energy is higher at higher temperature, the distance between I- and Q-structures is expected to be longer, and this is true as shown in Fig. 5. However, the paths connecting I- and Q-structures are not so simple at high temperatures. If the path were simple, then the distance to reach from the Q-structures to a state whose energy is higher by, say 1 kJ mol^{-1}, should not depend on temperature. Actually, its distance significantly depends on temperature. The slope from the bottom is small at higher temperature compared with that at lower temperature. The difference in the RMSD arises from two factors other than the thermal energy difference: (1) the change of the curvature along the initial displacement vector (including inflection points), (2) the deviation from the initial displacement vector by twisting the path. In fact, the steepest descent path at higher temperature is twisted more heavily than that at lower temperature and has a large number of the inflection points.

We choose six Q-structures along the trajectory generated by MD simulations at three temperatures to examine interbasin structures. We call these Q-structures the original basin centers, which are denoted by $\mathbf{R}_0$. Configurations around one of the original basin centers are generated by the normal mode excitations. To discern whether a generated configuration belongs to a basin other than the original basin, the steepest descent energy minimization is applied. The configuration space to be sampled depends on the mode energy. To reach the basins other than the original basin, the mode energy seems, in most of the cases, to be higher than the thermal energy. Therefore, the total mode energy covers a wide range from 0 to 100 kJ mol^{-1} with an interval of 0.125 kJ mol^{-1}. The mode energy is distributed such that the individual modes have the same mode energy. We examine 20 sets of configurations (10 independent sets and other 10 sets having opposite signs of q_i) at a given E_{mode}. Then, a standard quenching is applied to the excited states, $\mathbf{R}_e(=\mathbf{R}_0 + \Delta\mathbf{R}_e)$, for obtaining the local potential minimum, $\mathbf{R}_{\mathrm{Q}}$. Since the volume is fixed in the course of normal mode excitation and quenching, a low energy quenched configuration can be obtained even from a very high energy excited configuration. Thus, we examine a total of 1600×6 excited configurations at each temperature. Some of them fall into the same potential minimum. Plotted in Fig. 6 are typical examples of quenched potential energies as a function of $|\mathbf{R}_{\mathrm{Q}} - \mathbf{R}_0|$, at three temperatures along one of 10 normal mode directions. The vector $(\mathbf{R}_{\mathrm{Q}} - \mathbf{R}_0)$ generally deviates from the direction of $(\mathbf{R}_e - \mathbf{R}_0)$ due to quenching. Each figure includes the potential energies of 161 quenched configurations. The adjacent points are simply connected neglecting intervening barriers. At 298 K, the minima are widely distributed, which have the same energy levels as the original basin centers. The excitation and the subsequent quenching at 193 K almost always lead to the higher energy $\mathbf{R}_{\mathrm{Q}}$ while the potential energy in $\mathbf{R}_{\mathrm{Q}}$ is sometimes lower than that in $\mathbf{R}_0$ at 233 and 298 K. The potential energy of other basin at 193 K increases more harshly than that at 233 K (and 298 K) upon leaving away from the original basin center. The bottom region, which has the similar energy value to the original basin center at 193 K, is much narrower than that at 233 K (and 298 K), indicating smaller volume of this state in configuration space, and thus a lower configurational entropy.

4. Structure and Dynamics of Confined Water

Water in bulk phase is mostly characterized by its capacity of forming four hydrogen bonds each of which has almost the same interaction energy under low pressure. When some restrictions are imposed on the relative geometry of a pair of water molecules, such as confinement in nano space, this is no longer satisfied. Many differences in structure, dynamics, and even phase behavior are expected between bulk and confined water depending on the type of confinement. There are at

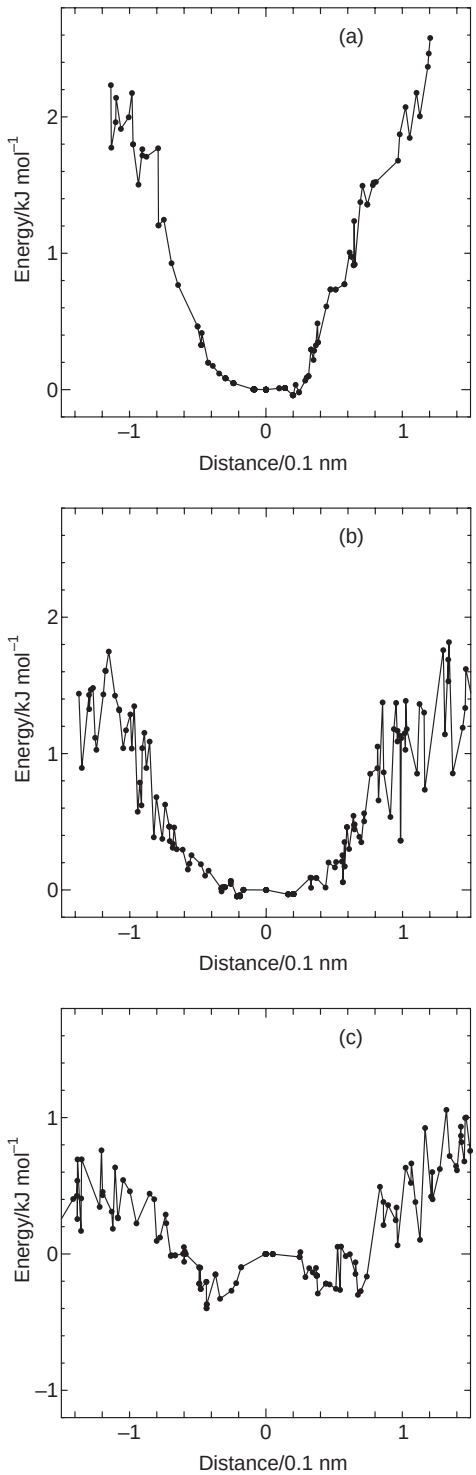

Fig. 6. Typical potential energy surface along a certain direction against distance in configuration space examined by the normal mode excitation. The temperatures in MD simulations are set to (a) 193 K, (b) 233 K, and (c) 298 K. The potential energy at the original minimum configuration is subtracted.

least thirteen crystalline phases in the phase diagram of bulk water, and remarkably all of them satisfy the ice rule except for ice X, i.e., every water molecule in each ice phase is fully hydrogen bonded.[54] This arises from a three-dimensional network-forming ability. We see that the network-forming ability persists even under heavy confinement since it is fairly strong and versatile.

We consider water under confinement by hydrophobic surfaces. At least one dimension of the confined space is of the order of a few molecular diameters. Examples are found in biological systems (e.g., water between and inside proteins, membranes, ion channels), micropore systems (e.g., water in zeolites, fullerenes, and porous glasses). The term "hydrophobic" means that no water molecules can form hydrogen bonds with the confining surfaces. If a hydrogen-bond network terminates at the surface, the potential energy per molecule increases by more than a few k_BT, and therefore, the properties of water are expected to be significantly altered, rather than to be merely perturbed. Especially in a low-temperature range where water has properties that are not common to other simple liquids, water could respond to the confinement quite differently, and thus the phase behavior of water under such confinement deserves attention.

Water is known to be confined in the carbon nanotube, but its properties in the quasi-one-dimensional space have not been as extensively studied as those of other substances. However, recent theoretical studies on water confined in a carbon nanotube and the experimental studies followed have demonstrated that the confined water freezes into a crystalline structure that has never been found in the bulk counterpart and exhibits continuous and discontinuous freezing transitions.[55–58] We also show MD evidence suggesting a new type of first-order phase transition—a liquid-to-bilayer crystalline or amorphous transition—above the freezing temperature of bulk water, depending on the type of pressure. These phase transitions are observed when water is confined in two hydrophobic sheets whose separation is only twice the diameter of water.[59–62] Liquid-like water having an imperfect random hydrogen-bonded network at high temperature undergoes a transition, under the normal pressure to the sheets, to a bilayer crystalline ice with a perfect network. An amorphous solid yields under the lateral pressure, which is made of various hydrogen-bonded polygons yet has no long-range order and thus is certainly amorphous ice. This transition can be shown via structure analysis as well as examination of thermodynamic properties.

4.1 Water in Carbon Nanotube. The inner region of the carbon nanotubes is an ideal space for examining properties of cylindrical quasi-one-dimensional water since it has simple and well-defined geometry. Although experiments focusing on confined fluids or solids inside carbon nanotubes have been conducted recently, the phase behavior of confined water has not been established thus far. There are, however, several computer simulation studies of water confined inside a carbon nanotube or a model cylindrical pore.[55,63–65] We emphasize the structure and the phase behavior of pure water at low temperatures studied by computer simulations.

Before examining phase behavior of water confined in the quasi-one-dimensional space, we find it possible to construct a perfect hydrogen-bond network in a quasi-one-dimensional space. The simplest network structure is a prism formed by n-gonal rings (Fig. 7). The standard ice rule is satisfied if every OH arm along each edge of the prism is oriented in one direction and every OH arm along each ring circulates in one direc-

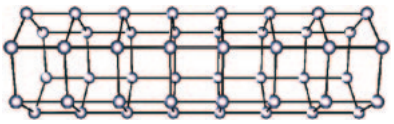

Fig. 7. Simplest form of a perfect network in a quasi-one-dimensional space. This example is a hexagonal-prism type network ($n = 6$).

tion. These quasi-one-dimensional hydrogen-bond networks have topologically perfect connectivity but suffer from heavy distortion away from the ideal orientation depending on n. In fact, it was shown that liquid water confined in a cylindrical space freezes into these ice forms with $4 \leq n \leq 7$, referred to as ice nanotubes due to the fact that their diameter is of nanometer scale. Moreover, it has been recently revealed that a similar ice form with $n = 8$ yields coexisting with small hydrophobic molecules accommodated in it.

Relative stability of the quasi-one-dimensional ice forms (as a function of their length) has been examined by the classical intermolecular potential models of water and by the ab initio quantum calculation,[66] and later, it was reinforced by more elaborated calculations.[67] When the number of molecules is small, the square ice form is found to be most stable, which is consistent with the previous studies of water clusters.[68] However, it is found that there is a crossover of stability from square to other ice forms with increasing the number of molecules; the pentagonal or hexagonal ice nanotube is found to be the most stable in the limit of infinite length.

The phase behavior of water confined in zigzag single-walled carbon nanotubes (SWCNs) has been studied by MD simulations and free energy calculations.[55] The diameter and helicity of a SWCN are uniquely defined by two integer indices, say, (m_1, m_2), and zigzag SWCNs are those with $m_2 = 0$; i.e., they are characterized by a single number m_1 or by $(m_1, 0)$. Five different nanotubes with indices $m_1 = 13$–18 are investigated, whose diameters range from 1.11 to 1.34 nm. For each system, a series of MD simulations starts from an arbitrary arrangement of water molecules at a fairly high temperature (e.g., $T = 350$ K) under a fixed axial pressure (e.g., $p_{zz} = 50$ MPa). After equilibration, phase behaviors are examined by cooling in steps. At sufficiently low temperatures, the liquid-like disordered structures turn into crystalline structures (Fig. 8), which are identified with the ice nanotubes anticipated to be stable in vacuum. No mobility of molecules indicates definitely that the low-temperature phases are indeed solids. The diameter of the carbon nanotube plays a crucial role in determining a size of ice nanotube. At $p_{zz} = 50$ MPa, a square ice nanotube forms in (13,0) and (14,0) carbon nanotubes, and pentagonal, hexagonal, and heptagonal ice nanotubes form in (15,0), (16,0), and (17,0) systems, respectively. In the largest (18,0) carbon nanotube, however, no crystalline structure has been found without a kind of "help gas" within the same simulation period as the others.

Two apparently opposite views are plausible as to freezing of confined water in the carbon nanotube. One is that freezing into ice nanotubes must be a first-order phase transition, as there is no liquid–solid critical point. The other is that any phase change in the carbon nanotube must be continuous as no first-order transition is expected in one-dimensional systems.

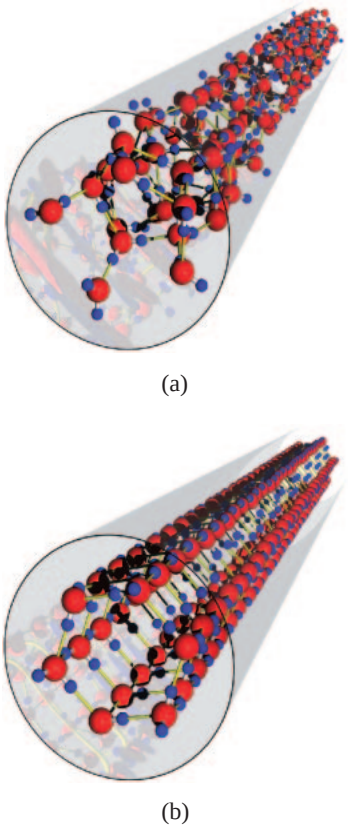

(a)

(b)

Fig. 8. Liquid (a) and solid (b) phases of TIP4P water confined in a (16,0) carbon nanotube. The solid phase has the hexagonal ice nanotube structure.

Plotted in Fig. 9 is the potential energy of water inside two different SWCNs as a function of temperature. For $m_1 = 15$ (not shown for $m_1 = 13$ and 14) at $p_{zz} = 50$ MPa, the potential energy decreases continuously with decreasing temperature while for $m_1 = 16$ (not shown for $m_1 = 17$) at the same pressure it jumps significantly at different temperature, which is called a hysteresis suggesting a first-order phase transition. The density and the structural order parameters exhibit the same continuous or discontinuous behavior, and the phase behavior also depends on the pressure. Under a higher pressure, water in a (15,0) carbon nanotube freezes into the hexagonal ice nanotube via a first-order-like phase transition (Note it freezes into a pentagonal form via a continuous transformation with a pressure of 50 MPa.). Thus, the results from the simulation do not agree with either view on freezing. Both continuous transformation and first-order-like phase transitions are expected depending on both thermodynamic (temperature, pressure) and mechanical (confinement) conditions.

More puzzling is the behavior of water confined in a (14,0) carbon nanotube. Upon cooling, it undergoes a continuous phase change to a square ice tube at 50 MPa, a first-order transition to a pentagonal ice tube at 200 MPa, and a continuous transformation to a pentagonal ice tube at 500 MPa. A set of isotherms for a (14,0) system in the pressure–volume plane shows that there exists a temperature below which the phase transformation becomes discontinuous and above which it is continuous (Fig. 10). Such a temperature is known as a critical temperature, usually found for gas–liquid phase equilibrium.

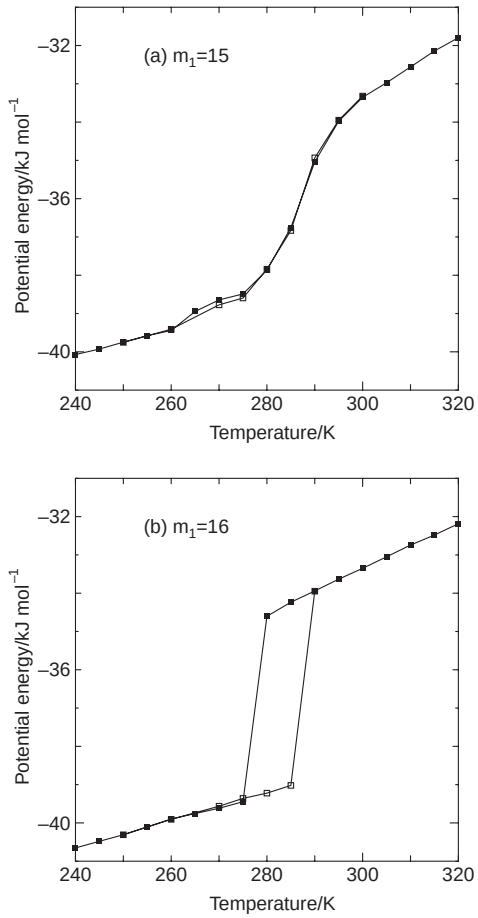

Fig. 9. Temperature dependence of the potential energy for TIP4P water confined in $m_1 = 15$ (a) and $m_1 = 16$ (b) carbon nanotubes. Filled and open symbols indicate the cooling and heating processes, respectively.

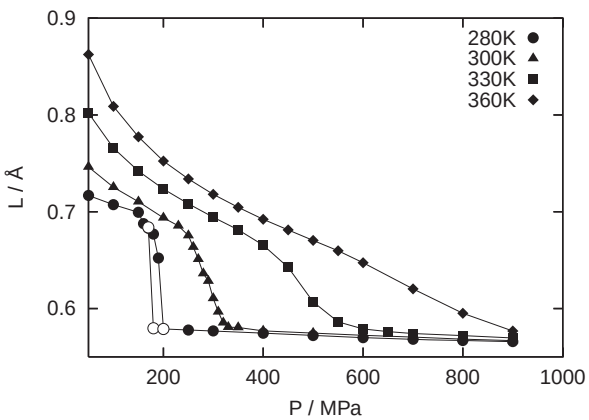

Fig. 10. Isotherms of the tube length per water molecule confined to the (14,0) carbon nanotube.

This suggests that the first-order phase boundary goes from low T and low p_{zz} to high T and high p_{zz} but terminates at the critical point (Fig. 11). These two phases separated by the boundary are the square and pentagonal ice tubes. We examine the two phases along the coexistence curve from a very low temperature to the critical one. It is found that both phases are solids in the lower temperature region, i.e., square and pentagonal ice nanotubes but the square phase gradually turns to be liquid-like with increasing temperature while the pentagonal phase remains solid-like. Since the boundaries between liquid-like and solid-like phases in both square and pentagonal structures are blurred, the well-known fact that no liquid–solid phase boundary terminates at a critical point does not hold in this confined system.

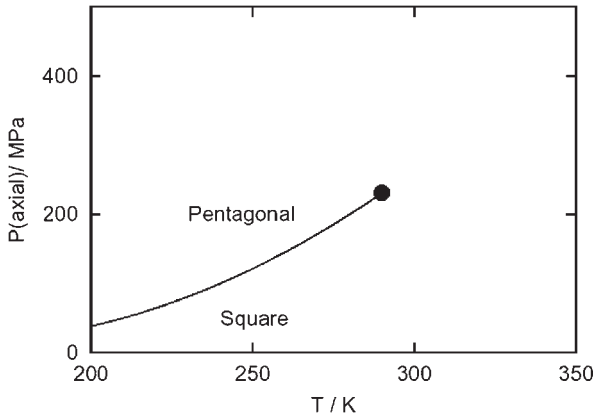

Fig. 11. Schematic phase diagram for water confined in a (14,0) carbon nanotube.

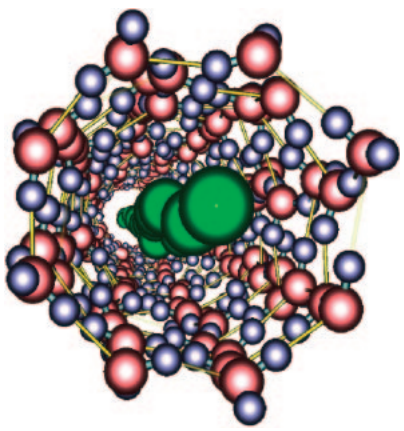

Fig. 12. Solid phases of TIP4P water confined in a (18,0) carbon nanotube with argon. The solid phase has the octagonal ice nanotube structure.

We further show that the ice nanotube in (18,0) carbon nanotube is spontaneously formed with guests, such as argon and methane, in the interior of the icetube as depicted in Fig. 12.[69] The occupancy of guest molecules is calculated from the approximate theory, which agrees well with the grandcanonical (GC) MC simulations for guest argon and methane but does not for neon. The stability of the ice nanotube relies on the attractive interaction with the guest molecules. Some small hydrophilic molecules may be accommodated in the ice nanotube if the attractive interaction (including weak hydrogen bonds) between water and the hydrophilic guest molecules is not so strong considering the recent experimental observation that even extra water molecules may exist inside the ice nanotubes.[58]

4.2 Water Confined in Slit Nanopores. The strong ability of water to form a hydrogen-bond network manifests itself not only in bulk and quasi-one-dimensional systems but also in

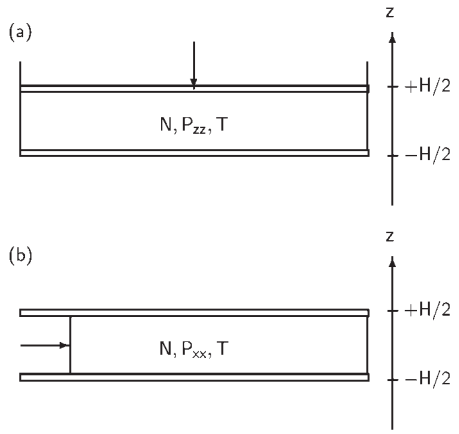

Fig. 13. Two different ways of confining a fluid in quasi-two-dimensional space. (a) $Np_{zz}T$-constant system, (b) $Np_{xx}T$-constant system.

quasi-two-dimensional systems. It is observed from MD simulations that water confined between two flat hydrophobic surfaces freezes into a bilayer ice crystal[60] or a bilayer amorphous ice.[62,70] These are associated with strong first-order transitions between two phases with a highly defective network and a (nearly) perfect network.

We examine a quasi-two-dimensional water focusing on the equilibrium conditions, structures at low temperatures, and similarities and differences between confined and bulk water. There are several ways to confine a fluid in a quasi-two-dimensional space. Let us consider two ways of confining a fluid in a quasi-two-dimensional space as shown in Fig. 13. The first is a closed system with a fixed area density N/A (number of molecules per unit area) under a fixed load p_{zz} (normal pressure). The second is a closed system with a fixed width H (separation distance between two surfaces) under a fixed lateral pressure p_{xx} and p_{yy}. The lateral pressure refers to the pressure tensor components parallel to the surfaces. Each system has a different equilibrium condition: a constant load in the first system is achieved by allowing volume change in the normal direction to the surfaces, and a lateral pressure in the second system is kept constant by allowing volume change in the lateral direction (There is another simple way in which a system is open to exchange water molecules.).

It is much harder to observe a freezing transition of bulk water with MD simulation than in real entity.[71] This fact can be taken advantage of when studying supercooled water without worrying about freezing. In contrast, it has been found that confined water in the constant-load system freezes rapidly enough to be observed by simulation under certain circumstances, that is, hydrophobicity of the surfaces between which water is confined with a fairly large load. The area density is chosen to be $21.2\,\mathrm{nm}^{-2}$. This means that there are about two water molecules per each $0.3\,\mathrm{nm} \times 0.3\,\mathrm{nm}$ area, which corresponds to a bilayer film of water. A restriction on load is necessary for confined water to be a homogeneous thin film. With these conditions satisfied, it is straightforward to observe the crystallization of confined liquid water when the high-temperature phase is cooled stepwise in MD simulation.[60] The observed phase change has the common features to an ordinary first-order phase transition. The freezing of confined water is

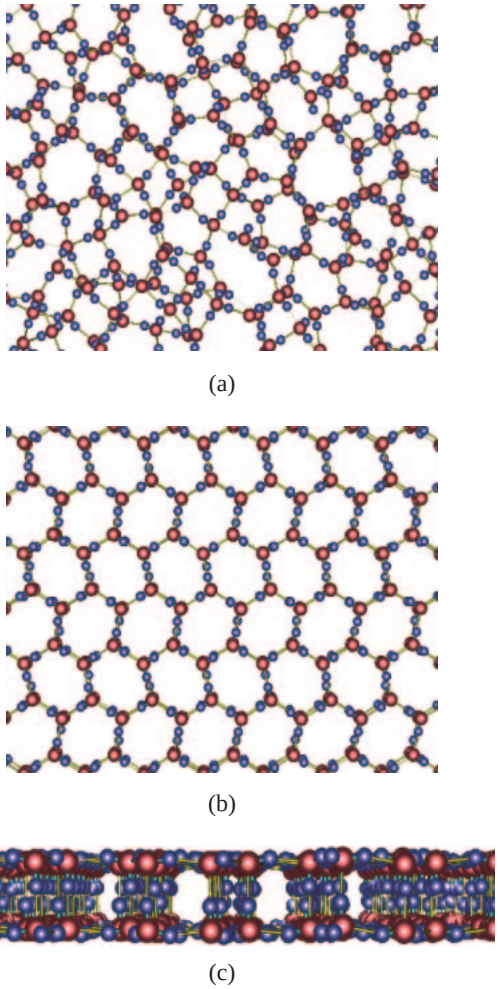

Fig. 14. Top views of the bilayer water (a) and ice (b) and side view of ice (c).

accompanied by large and abrupt decrease in potential energy ($4.6\,\mathrm{kJ\,mol}^{-1}$) due to the formation of a perfect hydrogen-bond network. Melting is observed at a temperature higher than the freezing temperature. In addition, confined water either contracts or expands as it freezes, depending on the constant load applied.

The crystalline solid phase has a quasi-two-dimensional perfect hydrogen-bond network of bilayer structure—the solid confined water is called the bilayer ice. Figure 14 shows views from a direction vertical and horizontal to the bilayer crystalline ice surface together with a view vertical to liquid. If we neglect the orientation of each molecule (or the locations of hydrogen atoms), the two layers have an identical distorted honeycomb lattice structure, and each node of which corresponds to an oxygen atom. Perfect connectivity of the hydrogen-bond network is realized in the bilayer lattice as follows: every water molecule is hydrogen-bonded to three neighbors in the same layer and vertically to the fourth neighbor in the other layer. The bilayer ice satisfies, in addition to the common ice rules, two extra ice rules, violation of which causes significant increase in potential energy and/or decrease in residual entropy. Owing to these rules, the residual entropy of the bilayer ice is calculated exactly as $S_c = (Nk_B/4)\ln 2$, which is 43% of the residual entropy of low pressure hexagonal ice (ice Ih) in bulk

phase, $S_c = (Nk_B)\ln(3/2)$.[72]

A phase transition in confined water is also observed when the slit-like pore is rigid (i.e., H is fixed) and a lateral pressure p_{xx} is applied. The resulting low-temperature phase is, however, an amorphous phase rather than the crystalline phase.[62] This phase behavior, which is unique to this confined system, is not due to the fact that the low-temperature phase is amorphous but that the liquid-to-amorphous phase change is a first-order transition rather than a glass transition. Temperature dependence of the potential energy (at $p_{xx} = 0.1$ MPa and $H = 0.87$ nm) shows two significant features of the first-order transition: (i) an abrupt change in energy (about 5 kJ mol^{-1}) within a small temperature range (around 270 K) and (ii) a hysteresis observed in the reversed heating process. Discontinuous changes are observed not only for the potential energy but also for the density, the normal pressure, and the structure. The amount of the energy change is comparable to that for freezing of bulk water to ice Ih and that for freezing of confined water to bilayer crystalline ice.[60] It is, however, much larger than that for the conjectured liquid–liquid transition of supercooled water.[18]

It is shown from long-time simulations that the diffusivity before and after the large drop in energy (at 275 and 270 K, respectively) differs by four orders of magnitude. This is again comparable to the change upon freezing of real water or TIP4P water to ice Ih. The drastic change in diffusivity is due to the phase change from liquid to solid (or solid-like) state. The structure of the solid (or solid-like) phase is found to be very similar to that of the bilayer crystalline ice. Almost every water molecule is hydrogen-bonded to its four neighbors: it is a bilayer structure and the spatial arrangement of oxygen atoms in one layer is superimposed on the other. It is clear that the substantial decrease in potential energy and the loss of fluidity at 270 K are due to the formation of a perfectly hydrogen-bonded network. The most important difference from the bilayer crystalline ice is its lack of periodicity in the two-dimensional structure (Fig. 15). In other words, the low-temperature phase is an amorphous solid. It is interesting to see that the two-dimensional hydrogen-bond networks of the bilayer ice and the bilayer amorphous are exact analogues of the honeycomb structure and the continuous-random network—the well-known two-dimensional models for crystal and glass.[73] The two-dimensional network structure of the bilayer amorphous ice has a wide distribution in the bond angle and several kinds of n-gonal rings: 77% hexagonal ($n = 6$), 11% pentagonal ($n = 5$), 11% heptagonal ($n = 7$) and 1% other ($n = 4$, 8, 9, and 10). Significant amounts of pentagonal and heptagonal rings indicate that these rings are not exceptional imperfections but rather characteristic constituents of the amorphous phase.

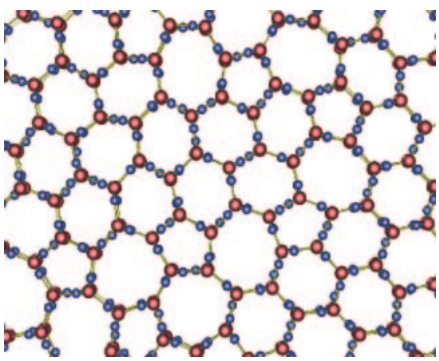

Fig. 15. Top view of the bilayer amorphous structure.

Existence of a phase boundary between two distinct amorphous or liquid phases of a pure substance is referred to as polyamorphism.[20,74] It has been reported that silicon,[75,76] carbon,[77,78] and phosphorus[79] exhibit polyamorphic liquid–liquid transitions. Polyamorphism in water has also been observed as the solid–solid transition between HDA and LDA by Mishima and co-workers.[13,14] Although still controversial, the liquid–liquid transition of water has been implied by molecular simulation in a metastable supercooled region inaccessible by experiment.[15–17] The transition of confined water in the rigid slit pore is a liquid–solid polyamorphic transition, and its first-order character is much clearer than that ever found in bulk water by simulation. This is also an uncommon example of a glass transition during which a liquid freezes into an amorphous solid via a first-order transition.

From MD studies of confined and bulk water, there are relationships among the three phases, i.e., a crystalline phase and two phases (disordered phases I and II) involved in polyamorphism. Let disordered phase I be the liquid phase stable in a temperature range between freezing and boiling points, and let disordered phase II be the liquid or amorphous phase that appears at lower temperature than the phase I and is usually metastable at any thermodynamic state. Then disordered phases I and II for confined water correspond to the liquid and the bilayer amorphous phase, respectively. For bulk water, disordered phases I and II are HDA and LDA phases (observed by experiments at a high-pressure region) or HDL and LDL phases (observed by simulations at a low-pressure region) respectively. Potential energy and structural properties of the three phases for each system are summarized in Table 3. There are two significant features common to confined and bulk systems:

(i) The potential energy difference between disordered phases I and II is greater than that between disordered phase II and the crystalline phase.

(ii) Upon the polyamorphic transition from disordered phase I to II, the distribution of molecules not having coordination number 4 nearly vanishes or substantially decreases.

In other words, concerning potential energy and structure of hydrogen-bond network, disordered phase II is much closer to a crystalline phase than to disordered phase I. Whether or not this holds for other substances with polyamorphism remains to be examined.

5. Thermodynamic Stability of Clathrate Hydrates

The solubility of apolar molecules in water is extremely low. For example, that of methane is about 10^{-5} in mole fraction at ambient temperature.[80] This is believed to be due to a large entropy decrease in hydration of an apolar solute. If a gas is pressurized, its solubility is sometimes drastically enhanced, and a solid–solution, called clathrate hydrate, is formed.[81,82] Clathrate hydrates are non-stoichiometric compounds made from water and guest molecules. They are stable only when guest molecules exist in their cages; several kinds

Table 3. Properties Characterizing the High-Density Amorphous Phase (HDA), the Low-Density Amorphous Phase (LDA), and the Crystalline Solid Phase in Both Quasi-Two-Dimensional System (Q2D) and Three-Dimensional Bulk System (3D)

	Potential energy/kJ mol^{-1}		4 H-Bond species/%		6-Membered rings/%	
Phase	Q2D	3D	Q2D	3D	Q2D	3D
HDA	−47.63	−53.5	73.1	80.6	35.4	46.4
LDA	−51.94	−54.9	99.7	88.3	76.7	62.8
Crystal	−52.98	−55.9	100.0	100.0	100.0	100.0

of empty polygons made from water molecules. Although there are no defects in the hydrogen-bond network of an empty clathrate hydrate structure, no clathrate hydrate without guest molecules has been found in nature. Thus, clathrate hydrates are stabilized by the (weak) attractive interactions between guest and water molecules. However, the guest species has some restrictions on its size. This arises from the fact that there are a limited number of cage types which encapsulate guest molecules without deviation of the hydrogen-bond lengths and angles from the ideal ones. In fact, the size of guest species has an upper bound and is smaller than a butane molecule. All of the cages are not necessarily occupied, and the cage occupancy depends on the temperature and the pressure of the guest compound in equilibrium with clathrate hydrate.

Thermodynamic stability has long been explained by van der Waals and Platteeuw (vdWP) theory which is valid under several assumptions.[83] Some of the assumptions in the original theory are not required with some of more elaborate treatments, and therefore, a more accurate evaluation can be made.[84–86] The free energy term arising from the coupling of the host with the guest molecules is important for large guest molecules such as propane. At higher pressures over 100 MPa the assumption of single-occupancy is no longer valid, and experimental work and theoretical calculations suggest that a larger cage can be occupied by more than one guest molecule. It is also shown that multiple occupancy can be treated in the framework of the vdWP theory by examining an argon hydrate at high pressures such as 500 MPa.[87]

5.1 Structure of Clathrate Hydrates. The clathrate hydrate structures, known as I and II,[81,82] differ from ice structures as shown in Fig. 16 and are stable only in the presence of guest molecules, which can be either hydrophobic or hydrophilic. The unit cells of both structures are cubic. The unit cell of the structure I contains 46 water molecules, and it is made from two kinds of cages: 2 smaller pentagonal dodecahedra and 6 larger tetrakaidecahedra. The unit cell of the structure II has 136 water molecules and is composed of 16 smaller pentagonal dodecahedra and 8 larger hexakaidecahedra. Some properties pertinent to the two kinds of clathrate hydrates are summarized in Table 4.[82] These cages are combined together by sharing faces as shown in Fig. 17. Larger guest molecules are found to be encaged in structure H, which is made of three types of polygons, but it is stable only when smaller cages are occupied by a smaller (different sort of) guest species.[88]

5.2 van der Waals and Platteeuw (vdWP) Theory and Its Extension. Let us begin with classical statistical mechanical (vdWP) theory, which accounts for stability of clathrate hydrates. This theory is applicable to any kind of hydrate, either type I or II and either simple or complex. It is assumed in this

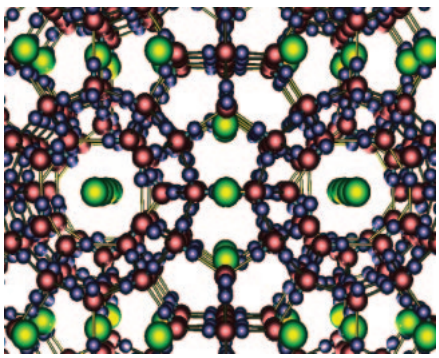

(a)

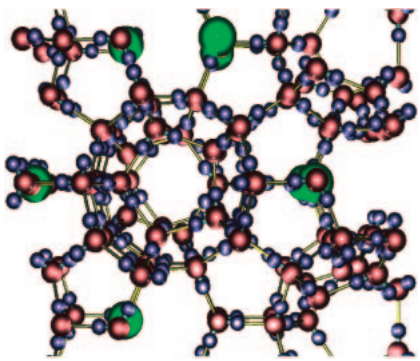

(b)

Fig. 16. Structure of clathrate hydrate I (a) and clathrate hydrate II (b).

Table 4. Properties Pertinent to the Unit Cells of Clathrate Hydrate I and II

Structure	I		II	
Number of water molecules	46		136	
Cell dimension/nm	1.203		1.731	
Cage type	Small	Large	Small	Large
Faces	5^{12}	$5^{12}6^2$	5^{12}	$5^{12}6^4$
Number of cages	2	6	16	8
Size of cage/nm	0.782	0.866	0.780	0.937

theory that (1) the cage structure is not distorted by the incorporation of guest molecules, (2) a cage is occupied by at most a single guest molecule and the free energy of cage occupancy is independent of the occupation of other cages, and (3) the guest molecule inside a cage moves in the force field of water molecules fixed at lattice sites and there is no coupling between host and guest molecular motions.[83] For simplicity, let

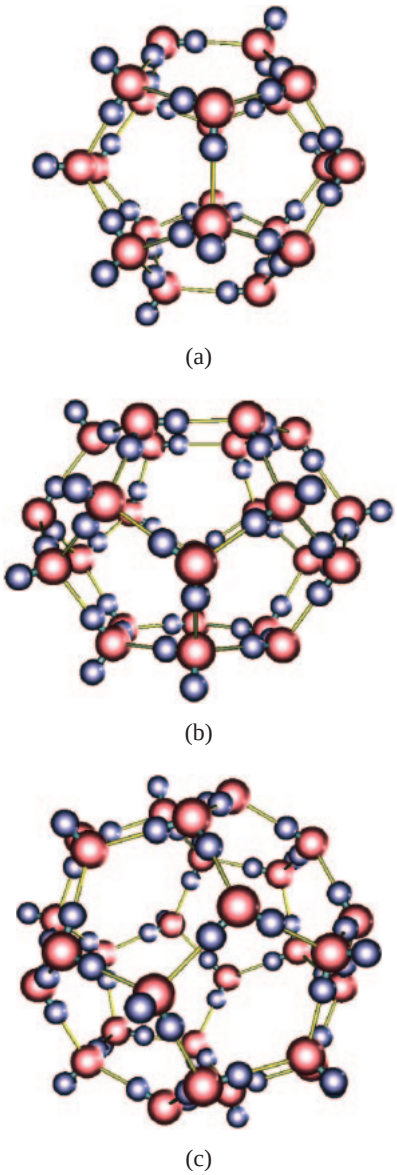

(a) (b) (c)

Fig. 17. Polygons to constitute clathrate hydrate I and II, pentagonal dodecahedron (a), tetrakaidecahedron (b), and hexakaidecahedron (c).

us consider a clathrate hydrate in which each cage accommodates one guest molecule of a single component with j_g degrees of freedom. The canonical partition function, Z, for a Hamiltonian $\mathcal{H}$ is given for N_g guest molecules having the symmetry number σ_g and N_w rigid rotor water molecules with $\sigma_w = 2$ as

$$Z = \frac{1}{\sigma_w^{N_w}\sigma_g^{N_g} N_w! N_g! h^{6N_w + j_g N_g}} \times \int_V \mathrm{d}\mathbf{r}_w^{N_w} \int \mathrm{d}\mathbf{p}_w^{N_w} \int_V \mathrm{d}\mathbf{r}_g^{N_g} \int \mathrm{d}\mathbf{p}_g^{N_g} \exp(-\beta\mathcal{H}), \quad (12)$$

where the integration in each coordinate $\mathbf{r}$ spans the whole volume denoted by V (the coordinates and the conjugate momenta include those associated with the orientational parameters if necessary). In Eq. 12, β stands for $1/k_\mathrm{B}T$ and h is the Planck constant. With the above assumptions, Z can be separated into two terms associated with the empty hydrate and the guests encaged in it as

$$Z = h^{-6N_w}\sigma_w^{-N_w} \int_v \mathrm{d}\mathbf{r}_w^{N_w} \int \mathrm{d}\mathbf{p}_w^{N_w} \exp(-\beta\mathcal{H}_w(\mathbf{p}_w, \mathbf{r}_w)) \times \sum h^{-j_g N_g}\sigma_g^{-N_g} \int_v \mathrm{d}\mathbf{r}_g^{N_g} \int \mathrm{d}\mathbf{p}_g^{N_g} \times \exp(-\beta\mathcal{H}_g(\mathbf{p}_g, \mathbf{r}_g; \mathbf{r}_w^0)), \quad (13)$$

where $\mathcal{H}_w$ stands for the Hamiltonian of host water and the Hamiltonian $\mathcal{H}_g$ includes both water and guest coordinates. The key in Eq. 13 is that the integration for guest coordinates is made for the fixed coordinates of the water molecules in a local energy minimum configuration, denoted by $\mathbf{r}_w^0$. The integration in each coordinate spans the smaller volume v in which each molecule vibrates but is not allowed to jump to the adjacent lattice site. The volume may be dependent on the molecular species. The sum in Eq. 13 is taken over all possible assignment of the guests to the available cages. The integral for the guest coordinate is individually evaluated under the above assumption to give the free energy term for single occupancy of the larger or smaller cage, $\exp(-\beta f_\mathrm{l})$ or $\exp(-\beta f_\mathrm{s})$. The number of ways to choose n_l single occupancies of larger cages and n_s single occupancies of smaller cages out of N_l larger and N_s smaller cages is

$$\binom{N_\mathrm{l}}{n_\mathrm{l}}\binom{N_\mathrm{s}}{n_\mathrm{s}}, \quad (14)$$

with $N_g = n_\mathrm{l} + n_\mathrm{s}$. Thus, the canonical partition function is given simply by

$$Z = \binom{N_\mathrm{l}}{n_\mathrm{l}}\binom{N_\mathrm{s}}{n_\mathrm{s}} \exp(-\beta A_w^0) \exp(-\beta n_\mathrm{l} f_\mathrm{l}) \exp(-\beta n_\mathrm{s} f_\mathrm{s}), \quad (15)$$

where A_w^0 is the Helmholtz free energy of the empty clathrate hydrate arising from the integral on host water in Eq. 13, which can be evaluated separately.

It is convenient to treat the clathrate hydrate as an open system, where the number of guest molecules is variable with a given chemical potential of the guest, μ. This is achieved by transforming from the canonical to the grandcanonical ensemble with respect to guest species. The grandcanonical partition functions obtained by multiplying $\exp(n_\mathrm{l}\beta\mu + n_\mathrm{s}\beta\mu)$ and taking sum over n_l and n_s as

$$\begin{aligned}\Xi &= \exp(-\beta A_w^0) \sum_{n_\mathrm{l}=0}^{N_\mathrm{l}} \binom{N_\mathrm{l}}{n_\mathrm{l}} \exp(\beta n_\mathrm{l}(\mu - f_\mathrm{l})) \times \sum_{n_\mathrm{s}=0}^{N_\mathrm{s}} \binom{N_\mathrm{s}}{n_\mathrm{s}} \exp(\beta n_\mathrm{s}(\mu - f_\mathrm{s})) \\ &= \exp(-\beta A_w^0)[1 + \exp(\beta(\mu - f_\mathrm{l}))]^{N_\mathrm{l}} \times [1 + \exp(\beta(\mu - f_\mathrm{s}))]^{N_\mathrm{s}}. \end{aligned} \quad (16)$$

Thus, the average number of guest molecules is calculated as

$$\langle N_g \rangle = \frac{\partial \ln \Xi}{\partial(\beta\mu)} = \frac{N_\mathrm{l} \exp(\beta(\mu - f_\mathrm{l}))}{[1 + \exp(\beta(\mu - f_\mathrm{l}))]} + \frac{N_\mathrm{s} \exp(\beta(\mu - f_\mathrm{s}))}{[1 + \exp(\beta(\mu - f_\mathrm{s}))]}. \quad (17)$$

The free energy of the empty hydrate is evaluated by the

Table 5. Free Energy for Double Occupancy of the Larger Cage (f_d), Single Occupancy of the Larger Cage (f_l), and Single Occupancy of the Smaller Cage (f_s) together with Chemical Potential Difference between Ice and Empty Hydrate ($\Delta\mu$) at Temperature T (K)[a)]

	T						
	213.15	223.15	233.15	243.15	253.15	263.15	273.15
f_d	−37.490	−38.762	−40.054	−41.365	−42.694	−44.041	−45.402
f_l	−25.699	−26.490	−27.286	−28.090	−28.899	−29.715	−30.585
f_s	−25.290	−25.882	−26.481	−27.089	−27.705	−28.329	−29.070
$\Delta\mu$	−0.799	−0.785	−0.772	−0.759	−0.745	−0.732	−0.719

a) Energy is in kJ mol^{-1}.

sum of the harmonic vibrational free energy, the potential energy of the system at temperature 0 K, U_q^0, and the configurational entropy as

$$A_w^0 = k_B T \int \ln(\beta\hbar\omega) g^0(\omega) \mathrm{d}\omega + U_q^0 - k_B T N_w \ln(3/2), \quad (18)$$

where $g^0(\omega)$ is the density of state for intermolecular vibrational motions.

At high pressures, some cages are occupied by two (or more) guest molecules. Extension to double occupancy of the larger cage is made as follows. The number of ways to choose n_l singly occupied and n_d doubly occupied larger cages and n_s singly occupied smaller cages is

$$\binom{N_l}{n_d}\binom{N_l - n_d}{n_l}\binom{N_s}{n_s}. \quad (19)$$

Thus, the canonical partition function is given by

$$\binom{N_l}{n_d}\binom{N_l - n_d}{n_l}\binom{N_s}{n_s} \exp(-\beta A_w^0) \times \exp(-\beta n_d f_d) \exp(-\beta n_l f_l) \exp(-\beta n_s f_s). \quad (20)$$

The grandcanonical partition function is again obtained by multiplying $\exp(2n_d\beta\mu + n_l\beta\mu + n_s\beta\mu)$ and taking sum over n_d, n_l, and n_s as

$$\begin{aligned}\Xi &= \exp(-\beta A_w^0) \sum_{n_d=0}^{N_l} \sum_{n_l=0}^{N_l - n_d} \binom{N_l}{n_d}\binom{N_l - n_d}{n_l} \\ &\quad \times \exp(\beta n_d(2\mu - f_d)) \exp(\beta n_l(\mu - f_l)) \\ &\quad \times \sum_{n_s=0}^{N_s} \binom{N_s}{n_s} \exp(\beta n_s(\mu - f_s)) \\ &= \exp(-\beta A_w^0)[1 + \exp(\beta(2\mu - f_d)) \\ &\quad + \exp(\beta(\mu - f_l))]^{N_l} [1 + \exp(\beta(\mu - f_s))]^{N_s}. \end{aligned} \quad (21)$$

The average number of guest molecules is calculated as

$$\langle N_g \rangle = \frac{\partial \ln \Xi}{\partial(\beta\mu)} = \frac{N_l[2\exp(\beta(2\mu - f_d)) + \exp(\beta(\mu - f_l))]}{[1 + \exp(\beta(2\mu - f_d)) + \exp(\beta(\mu - f_l))]} + \frac{N_s \exp(\beta(\mu - f_s))}{[1 + \exp(\beta(\mu - f_s))]}. \quad (22)$$

The actual integration for an atomic guest located at $\mathbf{r}_1$ with the mass m spans inside a cage and the free energy, f_l, is given (and f_s as well) by

$$\exp(-\beta f_l) = \left(\frac{2\pi m k_B T}{h^2}\right)^{3/2} \int_v \mathrm{d}\mathbf{r}_1 \exp[-\beta w(\mathbf{r}_1)], \quad (23)$$

where w is the interaction of a given guest with all the surrounding water molecules. The integration for two guest atomic coordinates $\mathbf{r}_1$ and $\mathbf{r}_2$ in a single cage is performed to give the free energy, f_d, as

$$\exp(-\beta f_d) = \frac{1}{2!}\left(\frac{2\pi m k_B T}{h^2}\right)^3 \int_v \mathrm{d}\mathbf{r}_1 \int_v \mathrm{d}\mathbf{r}_2 \times \exp[-\beta(w(\mathbf{r}_1) + w(\mathbf{r}_2) + \phi(\mathbf{r}_1, \mathbf{r}_2))], \quad (24)$$

where ϕ is the interaction between two guest molecules.

The equilibrium condition between ice and clathrate hydrate is given by

$$\mu_i = \mu_c, \quad (25)$$

where μ_i and μ_c denote the chemical potential of ice and clathrate hydrate. By subtracting the chemical potential of hypothetical empty clathrate hydrate, μ_c^0,

$$\mu_i - \mu_c^0 = \mu_c - \mu_c^0. \quad (26)$$

The chemical potential of ice is also calculated from Eq. 18. Each chemical potential is a function of pressure and temperature, but its pressure dependence in the left hand side is insignificant unless the pressure is very high. Therefore, we may neglect the pressure dependence (up to about 10 MPa), and the chemical potential for structure II is listed in Table 5 (that for structure I is higher by 0.1 kJ mol^{-1}). The right hand side is calculated to give

$$\mu_c - \mu_c^0 = -k_B T\{\alpha_l \ln[1 + \exp(\beta(\mu - f_l)) + \exp(\beta(2\mu - f_d))] + \alpha_s \ln[1 + \exp(\beta(\mu - f_s))]\}, \quad (27)$$

where α_l and α_s are the ratios of the numbers of the larger and smaller cages to the number of water molecules, respectively. This includes the chemical potential of the gas, which is significantly dependent on pressure.

5.3 Stability of Clathrate Hydrates Encaging Large Guests. The coupling between guest and host water molecules is not negligible for a large guest species, and a large guest molecule may give rise to modulation of the host water vibrational frequency. Then, the free energy of cage occupancy includes an extra contribution, which is not taken into account in the original vdWP theory. The assumption imposed on the vdWP theory can be eliminated for a spherical guest by the following method. We assume that the free energy, A, for a harmonic oscillator system is evaluated according to classical mechanical partition function for a harmonic oscillator as

$$A = k_B T \int \ln(\beta\hbar\omega) g(\omega) \mathrm{d}\omega + U_q - k_B T N_w \ln(3/2), \quad (28)$$

where $g(\omega)$ and U_q are defined in the same way as in Eq. 18 but for the whole clathrate system. The free energy of cage occupancy, f' is calculated by

$$f' = (A - A_w^0)/N_g. \tag{29}$$

For actual evaluation of f', an average over various cage occupancies is required.[84]

We first examine how the harmonic approximation works for occupation by a large guest molecule. Let us consider two extreme sizes, a large propane and a small argon. The propane molecule is approximated to a spherical LJ particle with size, σ, and energy, ϵ, parameters of 0.56 nm and 2.0 kJ mol^{-1}, respectively[89] in order to extract a significant contribution from the vibrational frequency shift of the host lattice caused by guest molecules. The LJ parameters σ and ϵ for argon are set to 0.34 nm and 1.0 kJ mol^{-1}, respectively.[89] For the water–guest interaction, we assume the Lorentz–Berthelot (LB) rule with the LJ parameters for oxygen atoms set equal to those for TIP4P water ($\sigma_{OO} = 3.2$ Å and $\epsilon_{OO} = 0.65$ kJ mol^{-1}).[5]

The potential energy of a guest propane molecule in structure II interacting with surrounding water molecules ($w(\mathbf{r})$ in Eq. 23) is calculated along three axes in Cartesian coordinates, and one of those energy curves is shown in Fig. 18a as a function of displacement of the guest molecule from the minimum energy position. The potential surface of propane is well fitted to a quadratic function of the molecular displacement from the cage center up to 20 kJ mol^{-1}, and therefore, the potential energy is expanded only to quadratic order. The potential energy curves of guest argon in the structure II hydrate are shown in Fig. 18b. In contrast to the propane, the potential energy curves are not quadratic even in the smaller cage. In the larger cage, the potential energy curve has two minima along each coordinate axis. Thus, a small guest molecule is only weakly coupled with the host water molecules. Therefore, separate integration for a smaller guest molecule is justified.[85] We consider a clathrate hydrate being in equilibrium with the fluid phase of guest species and low-pressure ice Ih, the latter of which is stable below a pressure of 200 MPa. The formation of clathrate hydrate is assumed to occur at fairly low pressure, i.e., below 10 MPa, so that the gas can be treated as an ideal or an imperfect gas by considering only the second virial coefficient.

Here, we show how the dissociation pressure at a given temperature is calculated for clathrate hydrates encaging propane or argon. The single particle partition function for argon turns out to give a correct dissociation pressure at temperature 273.15 K. On the other hand, the free energy, f based on Eq. 23 differs from f', which is the sum of the vibrational free energy difference and the interaction energy between water and guest molecules, Eq. 29 as tabulated in Table 6. This arises from the fact that the low-frequency modes associated with translational motions in the occupied hydrate by propane shift toward higher frequencies in comparison with empty hydrates. The shift is thermodynamically unfavorable for stabilizing the hydrate. According to the original assumptions made in the vdWP theory, the vibrational frequency shift should be negligible. However, its contribution to the free energy is positive and large in a real hydrate as in Table 6.

The dissociation pressure, p_d, is obtained from the intersection of two chemical potential differences, $\mu_c - \mu_c^0$ in Eq. 27

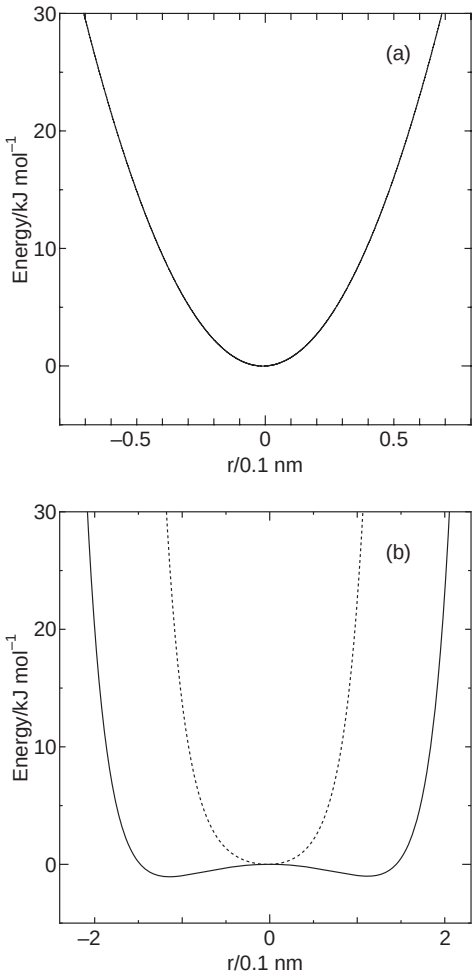

Fig. 18. (a) The potential energy of a guest propane molecule (approximated to a spherical LJ particle) in a large cavity of the clathrate hydrate II. (b) The potential energy of a guest argon atom in a large cavity (solid line) of the clathrate hydrate II and in a smaller cavity (dotted line).

Table 6. The Free Energy (kJ mol^{-1}) of a Guest Molecule f Based on the vdWP Theory and f' Based on the Intermolecular Vibration, and the Interaction Energy, u

	Free energy		
	Propane	Argon (large)	Argon (small)
u	−42.23	−11.43	−17.61
f	−48.93	−30.48	−28.97
f'	−45.21		

and $\mu_i - \mu_c^0$, the latter of which is calculated to be −0.72 kJ mol^{-1} at 273.15 K (Table 6). The occupation number per unit cell is 7.97 at $p_d = 0.56$ MPa, calculated from a classical mechanical partition function of harmonic oscillators. The occupation number calculated from Eq. 23 is 7.97 at $p_d = 0.10$ MPa. Clearly, Eq. 23 gives a lower dissociation pressure compared to Eq. 29. Therefore, the influence of the guest molecule on the host lattice is fairly large and cannot be neglected.[84,85,90] In the case of argon, guest atoms occupy both larger and smaller cages. The free energies of cage occupancy are calculated according to Eq. 29 and listed in Table 6. The calculated dis-

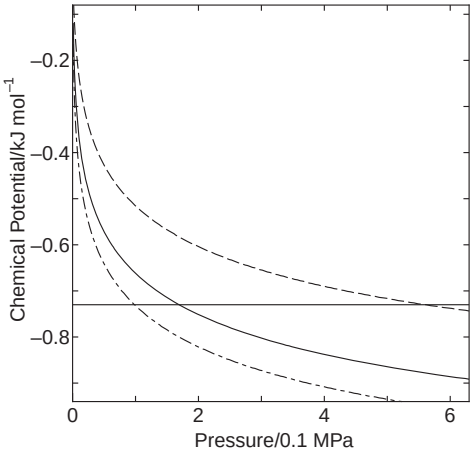

Fig. 19. Dissociation pressures of propane hydrate at 273.15 K. Solid line; nonspherical and anharmonic, dashed line; spherical and harmonic, dash-dot line; spherical and vdWP. Horizontal line; free energy difference between ice and empty clathrate hydrate II.

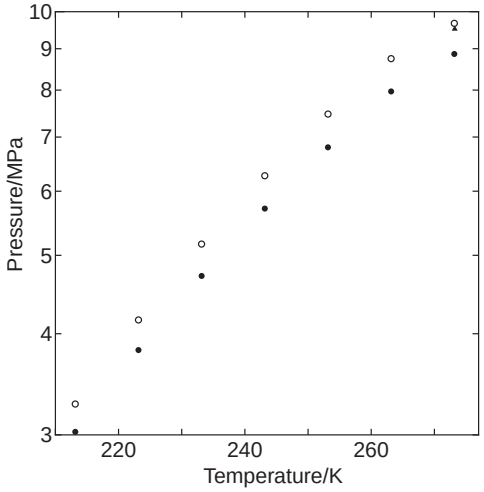

Fig. 20. Calculated temperature dependence of the dissociation pressure for argon clathrate hydrate together with experimental dissociation pressure (filled triangle). Clathrate hydrate is in equilibrium with realistic argon fluid (open circle) and hypothetical ideal gas (filled circle).

sociation pressure at 273.15 K is 10.4 MPa; the experimental value is 9.0 MPa.

The anharmonic contribution to the free energy from the host molecules is not negligible. It is especially significant when guest molecules are aspherical. This is because the rotational motions in the cages are essentially anharmonic. The anharmonic free energy can be calculated by several ways. Here, we show merely results from a revised method taking account of the anharmonic free energy to give a more accurate phase diagram. The anharmonic free energy is also evaluated by MC simulations with the Gaussian statistics.[86] The chemical potential difference between occupied and empty hydrates is plotted in Fig. 19 for nonspherical (harmonic + anharmonic terms) and spherical (harmonic term) guest propane molecules together with that calculated from the vdWP theory. The experimental dissociation pressure is 0.17 MPa,[82] which agree with the present result, $p_d = 0.17$ MPa. But, it is fairly different from the harmonic oscillator approximation explained above, $p_d = 0.56$ MPa, and from the original vdWP theory $p_d = 0.10$ MPa. The same method is also applied to ethane hydrate. The experimental dissociation pressure is 0.53 MPa,[82] which is very close to our result with the anharmonic free energy calculation, $p_d = 0.50$ MPa, but is different from the harmonic oscillator approximation, $p_d = 0.24$ MPa and from the vdWP theory, $p_d = 0.16$ MPa. The occupation number of the cages per unit lattice ranges from 5.5 to 5.6 among the three methods. The present extension of the vdWP theory results in much better agreement with experiment than any other method previously proposed as far as the dissociation pressures of propane and ethane guest molecules are concerned.

5.4 Double Occupancy in Argon Hydrate. It was experimentally shown that small molecules such as argon and nitrogen stabilize structure II rather than structure I.[91] Moreover, experimental evidence suggests that the larger cages in structure II hydrate can accommodate two small molecules, such as nitrogen, in the intermediate pressure range (lower than 400 MPa).[92] We examine the dissociation pressure and the pressure dependences of the cage occupancies at several temperatures, 213.15 to 273.15 K. The free energies of cage occupancy, f_l and f_s, are calculated according to Eq. 23.[93] The free energy of double occupancy is obtained in the same way, Eq. 24. For efficient evaluation of the value, care is taken of the fact that the 6-dimensional character of the integrand appears only in the guest–guest interaction, ϕ, which is evaluated much faster than w. The free energies of cage occupancy, f_l, f_s, and f_d are given in Table 5.

The chemical potential of the imperfect gas (fluid) is calculated as follows. The equation of state for LJ fluids (pressure, p) has been well established as $p(T, \rho)$ where ρ is the number density.[94] The free energy (per molecule) f_g at T and ρ is given by the non-ideal and the ideal parts as

$$f_g = \int_0^\rho (p - \rho k_B T)/\rho^2 \mathrm{d}\rho + k_B T[\ln \rho(h^2/2\pi m k_B T)^{3/2} - 1]. \quad (30)$$

Since we deal with one-component system in calculating the chemical potential of the gas, μ, it is simply given by

$$\mu(T, p) = f_g + p/\rho, \quad (31)$$

after inversion of the equation of the state as a function of p.

The temperature dependency of the dissociation pressure is shown in Fig. 20, and it is almost the same as the previous calculation neglecting double occupancy.[93] Agreement with experiment is excellent in view of the simple potential function and the conventional combining rule.[95] A more realistic treatment of argon gas gives rise to slightly better agreement with the experimental observation but the difference in dissociation pressure from the ideal gas chemical potential is less than 0.08 MPa. Therefore, argon gas can be regarded as an ideal gas in the low pressure region (below 10 MPa). The cage occupancy is plotted in Fig. 21. Approximately 80 and 90% of smaller and larger cages are occupied, respectively. At any temperature, the occurrence of double occupancy is less than 1%, and therefore, only single occupancy is dominant around

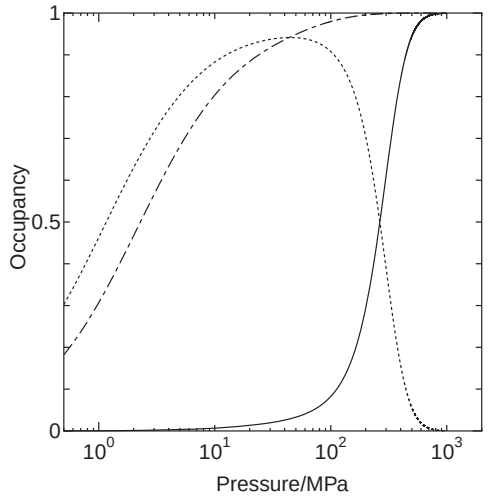

Fig. 21. Cage occupancy ratio of guest argon atoms in equilibrium with realistic argon gas. Solid line; double occupancy in larger cage, dotted line; single occupancy in larger cage, dash-dot line; single occupancy in smaller cage.

the dissociation pressure. Double occupancy gradually increases with increasing gas pressure, up to 10 MPa, and then, a sharp increase is seen. Double occupancy dominates over single occupancy of larger cages when the gas pressure exceeds 270 MPa at 273.15 K. If the gas is treated as an ideal gas, the occupancy of smaller cages is almost the same but the occupancy of larger cages is significantly different, and cross-over occurs at a pressure higher than 1 GPa, which is 4 times higher than the case of a real gas (fluid). Some experimental evidence suggests double occupancy takes place at around 400 MPa prior to the transition from structure II to structure H.[96–99] Agreement with experiment is expected only when argon is treated not as an ideal gas but as a more realistic LJ fluid.

Further extension to multiple occupancy is easily made by considering that individual guest molecules of the same kind cannot be distinguished in a single cage although numerical task becomes increasingly heavier. The relevant grandcanonical partition function is given as

$$\Xi = \exp(-\beta A_w^0) \prod_k \left[\sum_{n=0} \exp(\beta(n\mu - f_{kn})) \right]^{N_k}, \qquad (32)$$

where f_{kn} is the free energy of occupancy of type-k cage by n guest molecules out of N_k cages in clathrate hydrate. The average guest number is calculated as

$$\langle N_g \rangle = \frac{\partial \ln \Xi}{\partial(\beta\mu)} = \sum_k \frac{N_k \left[\sum_{n=1} n \exp(\beta(n\mu - f_{kn})) \right]}{\left[\sum_{n=0} \exp(\beta(n\mu - f_{kn})) \right]}. \qquad (33)$$

The integration for n (atomic) guest coordinates in a single cage is performed to give the free energy f_{kn} as

$$\exp(-\beta f_{kn}) = \frac{1}{n!} \left(\frac{2\pi m k_B T}{h^2} \right)^{3n/2} \times \int_v \prod_i^n d\mathbf{r}_i \exp\left[-\beta \left(\sum_i^n w_k(\mathbf{r}_i) + \sum_{i<j}^n \phi(\mathbf{r}_i, \mathbf{r}_j) \right) \right]. \qquad (34)$$

The above extension is used for clathrate hydrates at high pressure, i.e., structure H in which the largest cage can accommodate up to 5 argon atoms.

5.5 Other Theoretical Calculations on Clathrate Hydrates. The thermal conductivity of clathrate hydrate is roughly 20% that of ice near the melting point and is one order of magnitude smaller at low temperatures below 150 K.[100,101] The thermal conductivity of ice is inversely proportional to temperature as is the case of normal crystal. On the other hand, that of the hydrate is proportional to temperature although its temperature dependence is not so clear. MD simulations have been performed to account for the anomalous conductivity.[102]

Gas mixtures of methane and ethane form structure II clathrate hydrates in certain composition ranges despite the fact that pure methane and pure ethane gases form the structure I hydrate.[103–105] Optimization of the interaction potential parameters for methane and ethane is attempted so as to reproduce the dissociation pressures of each simple hydrate containing either methane or ethane alone. An account for the structural transitions between type I and type II hydrates upon changing the mole fraction of the gas mixture is given on the basis of the vdWP theory with these optimized potentials.[106] There are three important factors to explain which form, structure I or II, of the methane + ethane mixed hydrate is more stable. First, empty structure II hydrate has a lower chemical potential value than an empty structure I hydrate, second, the ratio of the number of larger cages to the number of water molecules for structure I is much larger than that for structure II, and third the free energy of the larger cage occupancy for structure II is lower than that for structure I for both methane and ethane. The first and third factors contribute to stabilizing structure II hydrate, while the second one contributes to stabilizing structure I hydrate. The preferential structure for a given condition is determined by competition among these three factors.

6. Thermodynamic Properties of Ices

Stable morphology of crystalline states has been predicted by means of MD simulations with variable cell size and shape, proposed by Parrinello and Rahman.[107] This method is a powerful tool to reproduce or predict phase transitions among various crystalline forms. These transitions, however, correspond to the limit of mechanical stability. Thus, the true phase transition point should be evaluated by calculating the free energies of crystalline structures in order to draw a phase diagram of various crystalline forms. The free energies of low-pressure ice Ih and cubic ice (ice Ic) are calculated from various components separately: the interaction energy at temperature 0 K, the vibrational free energy, and the configurational entropy arising from disordering of protons. This enables us to evaluate the thermodynamic stability of these ices at low temperatures from only intermolecular interactions and to elucidate higher stability of ice Ih over ice Ic.

The thermal expansivity of ice Ih is negative below temperature 70 K,[108] which is also observed for tetrahedrally coordinated compounds such as silica.[109] Although the negative thermal expansivity was discovered more than four decades ago, it has not been established whether this negative thermal expansivity has a common origin to the tetrahedral structure in low temperature. In theoretical treatment via the Grüneisen rela-

tion, frequencies of some of vibrational modes must modulate to higher frequency side when the crystal is dilated as described below. Moreover, the heat capacity of such a mode must vary significantly against temperature change. Thus, a standard classical statistical mechanical treatment fails to account for this unusual thermal expansivity.

It is not surprising that most of thermodynamic and dynamic properties of clathrate hydrate are similar to those of ice since the interaction between guest and host water molecules is not strong enough to alter those properties which seem to be mostly originated from the hydrogen bonds. However, the thermal expansivity of clathrate hydrates is different from that of ice.[82] Other peculiar property of ice Ih is also investigated, which is related to proton-ordering.

6.1 Free Energy Calculation and Relative Stability of Ice Ih and Ic. The thermal expansivity of crystalline solid is evaluated by calculation of its Helmholtz free energy, $A(T, V)$, which is a function of the temperature, T, and the volume, V. The free energy is expressed by

$$A(T, V) = U(V) + F(T, V) - TS_c, \tag{35}$$

where $U(V)$, $F(T, V)$, and S_c are the potential energy of the system in equilibrium position at temperature 0 K, the vibrational free energy, and the configurational entropy, which is approximately $Nk_B \ln(3/2)$ for an ice of N water molecules.[72] If the anharmonic vibrational free energy is ignored, $F(T, V)$ is replaced by the harmonic vibrational free energy $F_0(T, V)$. The anharmonic nature still remains in $U(V)$ and in $F_0(T, V)$ through the volume dependence of the intermolecular vibrational modes, ν_i. The harmonic vibrational free energy is given by

$$F_0(T, V) = k_B T \sum_i \ln[2 \sinh(\beta h \nu_i / 2)]. \tag{36}$$

It is obtained by a simple average over the generated configurations. Once they are obtained, evaluation of the harmonic free energy, F_0, is straightforward. The potential energy $U(V)$ is dependent only on the volume but $F_0(T, V)$ is a function of both the volume and temperature. Since we are interested in the stability of ice Ic relative to ice Ih, the configurational entropy part completely cancels out. It is reasonable to assume that the anharmonic free energy difference can also be neglected since the anharmonic contribution is expected to be small at low temperatures. A similar method including anharmonic free energy is applied to estimate the melting temperature of TIP4P ice Ih, which turns out to be located around 230 K at atmospheric pressure.[110–112]

If the volume at a constant pressure can be calculated as a function of temperature, it is straightforward to evaluate the thermal expansivity. Instead of MD or MC simulation, we obtain the equilibrium volume by minimizing the Gibbs free energy at a given temperature. The Gibbs free energy ($G(T, p) = A(T, V) + pV$) has a minimum value against volume variation at a given temperature T and pressure p. The volume is varied isothermally while the pressure is fixed to a constant value. The Gibbs free energies at three cell sizes are calculated: The linear scale factors of the cell, ξ, are chosen to be 1 ± 0.015. In ice Ih, the ratios a/c and b/c are fixed to constant values and the basic cell is uniformly expanded or shrunk. Since the volume is initially chosen to be close to the equilibrium one, the equilibrium volume, at which the free energy has a minimum value is expected to fall within $(1 \pm 0.045)V$ for most temperatures. The minimum free energy is accurately calculated by fitting those three values to a quadratic function of volume at a given temperature and pressure. The equilibrium density is calculated together with the Gibbs free energy. Then, we compare thermodynamic stability of two sorts of ices. Once the volume is obtained as a function of temperature, it is simple to calculate the thermal expansivity.

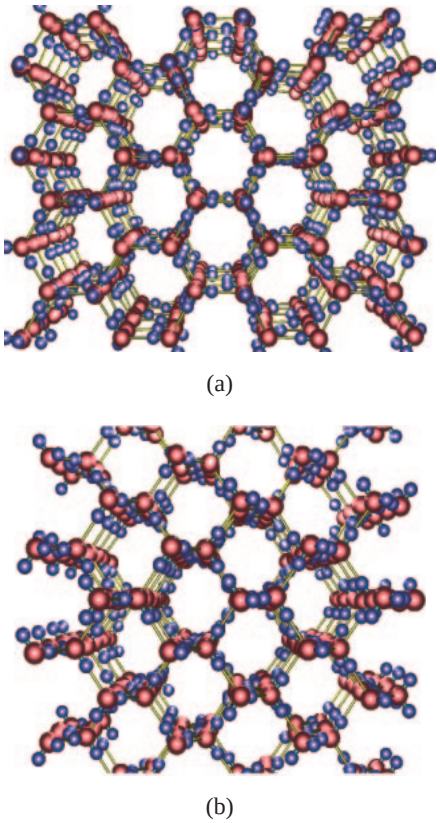

Fig. 22. Structure of ice Ih (a) and ice Ic (b).

Normal water under the ambient condition freezes not into ice Ic but into ice Ih. Ice Ih has a trygimite structure while ice Ic possesses a diamond structure as displayed in Fig. 22. Most of the quantities concerning the hydrogen bonds for ice Ih are similar to those of ice Ic.[1] Both ice Ih and ice Ic structures are composed of hexagonal rings and the only way to stack them is different from each other. Ice Ic is metastable and observed under limited conditions. The metastable nature of ice Ic has been explained by experimental evidence that ice Ih is energetically more stable than ice Ic ($\simeq 50\,\mathrm{J\,mol^{-1}}$).[113] However, water always nucleates to ice Ic in preference to ice Ih from high pressure ices when decompressed at low temperature[114] or from liquid state to an ice cluster.[115]

In Fig. 23, the free energies (a) and energies (b) for both ice Ih and Ic to 273 K are plotted against temperature. The energy is defined as the sum of the interaction energy $U(V)$ and the vibrational energy $E(T, V)$. The latter is calculated according to

$$E(T, V) = 1/2 \sum_i h\nu_i \coth(\beta h \nu_i / 2). \tag{37}$$

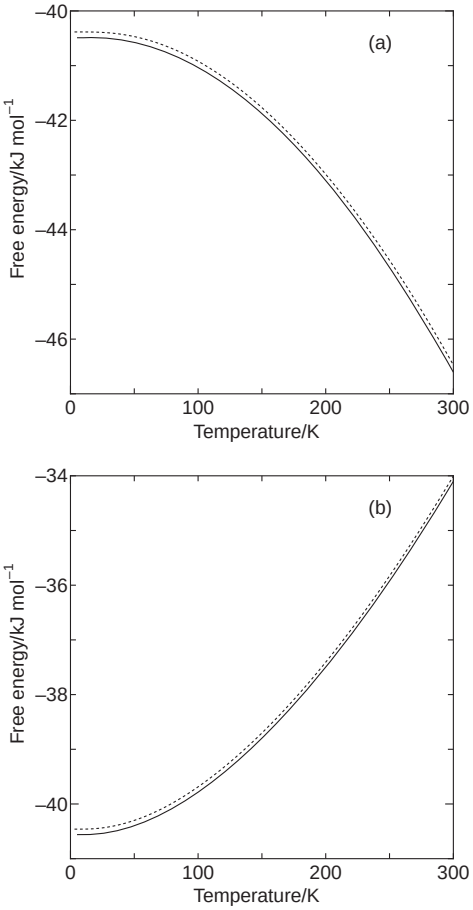

Fig. 23. (a) Temperature dependence of the free energy for ice Ih (solid line) and ice Ic (dotted line), where contributions from the configurational entropy and anharmonic vibrations are omitted. (b) Temperature dependence of the energy which is defined as the sum of the interaction energy at its minimum structure and vibrational energy for ice Ih (solid line) and ice Ic (dotted line).

The free energy difference is small but increases with increasing temperature, i.e., it increases from 0.107 kJ mol^{-1} at 53 K to 0.128 kJ mol^{-1} at 273 K. On the other hand, the energy difference has different temperature dependence though very small; it is 0.111 kJ mol^{-1} at 53 K and 0.105 kJ mol^{-1} at 273 K.[116,117] The relative stability reasonably agrees with the experimental observations, and the vibrational free energy plays a certain role in the temperature dependence of the total free energy as well as the surface entropy.[118]

6.2 Grüneisen Relation and Thermal Expansivity of Ice Ih. Thermodynamics relates the linear thermal expansivity α with the free energy

$$3\alpha = (\partial \ln V/\partial T)_p = -\kappa_T \partial^2 A/\partial T \partial V, \tag{38}$$

where κ_T is the isothermal compressibility, which is always positive for any stable system. The linear thermal expansivity is given as

$$\alpha = \gamma C_v \kappa_T / 3V, \tag{39}$$

where C_v and γ are the heat capacity and the Grüneisen parameter, respectively. The heat capacity is given by the sum

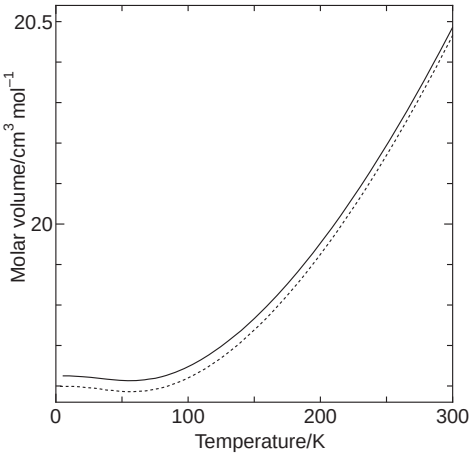

Fig. 24. Molar volume of ice Ih (solid line) and Ic (dotted line) as a function of temperature.

of the heat capacities of the individual modes as

$$C_v = \sum_i C_i. \tag{40}$$

Here, C_i is the heat capacity of i-th mode, which is given by

$$C_i = k_B(\beta h\nu_i)^2 \exp(\beta h\nu_i)[\exp(\beta h\nu_i) - 1]^{-2}. \tag{41}$$

The Grüneisen parameter is defined using C_i by

$$\gamma = \sum_i \gamma_i C_i \Big/ \sum_i C_i, \tag{42}$$

where γ_i is

$$\gamma_i = -(\partial \ln \nu_i/\partial \ln V). \tag{43}$$

Instead of the quantum mechanical partition function for a harmonic oscillator, Eq. 36 may be replaced by the classical partition function as

$$F_0^c(T, V) = k_B T \sum_i \ln(\beta h\nu_i). \tag{44}$$

However, this gives rise to a constant heat capacity, k_B, for any harmonic vibrational motion. In light of Eq. 42, the thermal expansivity cannot change its sign in classical system since C_v, κ_T, and V are all positive and γ is no longer dependent on temperature. Therefore, use of Eq. 36 is essential to account for the change in the sign of α in low-temperature regime.

The molar volumes of the two ice forms are plotted in Fig. 24. The volumes of ice Ih and Ic increase with increasing temperature above 60 K. However, both have negative slopes below 60 K. Thus, the thermal expansivity plotted in Fig. 25 is negative for ice Ih (also ice Ic), which reasonably agrees with experimental evidence. The calculated thermal expansivity for ice Ih (0.72×10^{-4} K^{-1}) at 200 K (average over a, b, and c axes) is somewhat larger than the experimental value, (0.56×10^{-4} K^{-1}).[119]

The dilation of the volume at 0 K induces normally a shift in the mode frequency to a lower value such that the vibrational free energy becomes lower while the interaction energy becomes higher. The equilibrium volume is determined by those two different contributions. However, frequencies of some modes must have a different volume dependence in order for

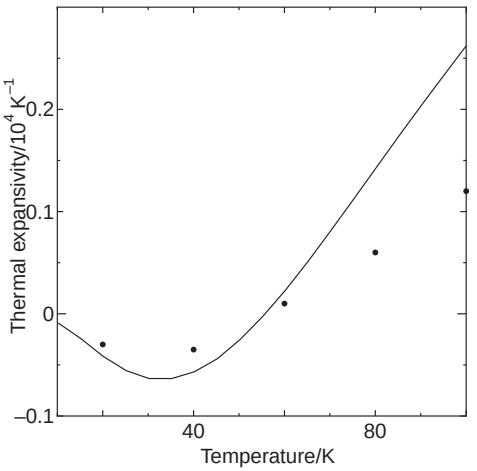

Fig. 25. Thermal expansivity of ice Ih as a function of temperature together with experimental results (filled circle).

α to change its sign. To examine the positivity of γ_i, the following analysis is made. Let **K** be the mass weighted force constant matrix ($\mathbf{K} = \mathbf{m}^{-1/2}\mathbf{V}\mathbf{m}^{-1/2}$). It is diagonalized to give $\mathbf{K}_\mathrm{d}$ as

$$\mathbf{K}_\mathrm{d} = \mathbf{U}\mathbf{K}\mathbf{U}^\dagger, \tag{45}$$

where **U** is a unitary matrix. First, we obtain **U** for $\xi = 1$. Next, Eq. 45 is applied to $\xi = 1 \pm 0.015$ with the matrix, **U**. The small change in the volume does not alter the characters of individual modes. Indeed, this procedure is successfully applied and all the modes for $\xi = 1 \pm 0.015$ are real. There are many low frequency modes which have negative γ_i. The frequency of those modes are lower than 60 cm^{-1}. Most of the modes in this frequency range are associated with bending motions of three hydrogen-bonded molecules; a bending of O···O···O. The negative thermal expansivity of ice at low temperature arises from the unusual negative γ_i and from larger heat capacity of these modes relative to those of other modes having positive γ_i. The modes having negative γ_i correspond to the bending motions of three water molecules hydrogen bonded. That the frequencies of these modes are low is a key to the negative thermal expansivity.

The thermal expansivity of ethylene oxide clathrate hydrate is nearly twice as large as that of ice.[119–121] This difference has been explained by a difference in either host water or guest molecules. The former is a difference in the arrangement of host water molecules; ice is made from hexagonal puckered rings while clathrate hydrate is composed of planar hexagonal and pentagonal rings. The latter is an effect of guest molecules; the coupling of guest and host water or the guest vibrations, or both. We have examined the origin of the unusually large thermal expansivity of xenon clathrate hydrate (structure I). Xenon interaction is described by an LJ potential whose parameters are $\sigma = 0.405$ nm and $\epsilon = 1.92$ kJ mol^{-1}.[89] The thermal expansivity for the occupied hydrate at 200 K is 1.04×10^{-4} K^{-1}.[122] This is comparable to the experimental value, 0.77×10^{-4} K^{-1} (for ethylene oxide hydrate structure I).[123] The calculated thermal expansivity for ice Ih, 0.72×10^{-4} K^{-1}, at 200 K is smaller than that of the occupied clathrate hydrate. It is interesting that the calculated thermal expansivity for an empty hydrate, 0.73×10^{-4} K^{-1}, is almost the same as that for ice Ih. Although a difference in thermal expansivity between experimental and theoretical values is not so small, the calculated value for occupied hydrate is much larger than that for ice Ih and empty hydrate. A more detailed study shows that the main source of the larger thermal expansivity is the vibrational motions of guest molecules inside the cages which dominates over the guest interaction energy and that the guest interaction term rather diminishes the thermal expansivity.[122] The effective potential energy surface of a guest molecule becomes harmonic with increasing temperature. This seems to undermine the large difference in the thermal expansivity between clathrate hydrate and ice with increasing temperature.

6.3 Debye–Waller Factor of Ice Ih and Migration of Water Molecules. It is experimentally known that the slope of the Debye–Waller (DW) factor for oxygen atoms in ice Ih changes at higher temperatures.[124] The DW factor is examined by MD simulations for twenty five different proton-disordered ice Ih configurations, each containing 288 molecules. Each production run is 15 ns except for one configuration (30 ns). The DW factor that originated from the harmonic vibrations is calculated by the following statistical mechanical treatment. The system is described by a collection of harmonic oscillators with reference to the corresponding local energy minimum structure. The Hamiltonian of ice is assumed to be harmonic as

$$\mathcal{H} = \sum_i \left(n_i + \frac{1}{2}\right) h\nu_i + U_q, \tag{46}$$

where U_q is the potential at the minimum, ν_i is the frequency of the i-th mode, and n_i is the quantum number for i-th vibrational mode with its frequency ν_i. Since the coordinates $\Delta\mathbf{r}$ in real space are related to the collective coordinate **q** by

$$\Delta\mathbf{r} = \mathbf{m}^{-1/2}\mathbf{U}^\dagger\mathbf{q}, \tag{47}$$

we use **S**, the square root of the inverse mass matrix $\mathbf{m}^{-1}$, which may contain finite off-diagonal elements denoting the ij-element of $\mathbf{U}^\dagger$, and **S** by u_{ij} and s_{ij} respectively, to obtain

$$\langle \Delta r_i^2 \rangle = \sum_{j,k,l} s_{ij} s_{ik} u_{jl} u_{kl} \langle q_l^2 \rangle. \tag{48}$$

The angular brackets denote thermal average. The average of the l-th normal coordinate $\langle q_l^2 \rangle$ is defined by

$$\langle q_l^2 \rangle = \mathrm{Tr}(\rho(\mathcal{H}) q_l^2), \tag{49}$$

where ρ is the density matrix of the entire system. Since all the modes are completely independent, $\langle q_l q_m \rangle = 0$ for $l \neq m$, and we obtain

$$\begin{aligned} \langle q_l^2 \rangle &= \sum_{n_l} \rho(n_l) \langle n_l | q_l^2 | n_l \rangle \\ \rho(n_l) &= \exp(-n_l \beta h \nu_l)[1 - \exp(-\beta h \nu_l)] \\ \langle n_l | q_l^2 | n_l \rangle &= h\left(n_l + \frac{1}{2}\right) 4\pi^2 \nu_l. \end{aligned} \tag{50}$$

In classical statistical mechanics, the mean-squared displacement of the l-th vibrational mode is expressed in terms of its frequency ν_l as $\langle q_l^2 \rangle = k_\mathrm{B}T/(2\pi\nu_l)^2$; substituting this relation in Eq. 50 leads to the mean-squared displacement of the individual molecules.

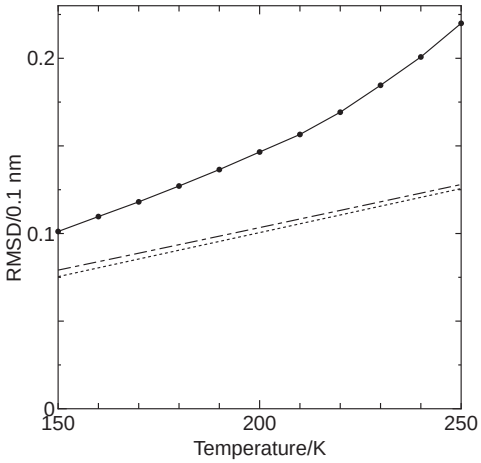

Fig. 26. The mean-squared displacement (MSD), i.e., the Debye–Waller factor for hexagonal ice averaged over 25 proton-disordered configurations is plotted versus temperature. The solid line denotes the DW factor obtained from MD simulation, dotted line denotes the corresponding DW factor in the classical harmonic approximation, while the dot-dash is the quantum harmonic approximation.

Shown in Fig. 26 is the DW factor as a function of temperature for TIP4P ices. There is a change in slope of the DW factor around 200 K. The larger DW factor does not mean melting of the ice; the DW factor does not increase as the simulation proceeds implying that the system remains solid. Thus, the break in DW factor is real and it could correspond to a break observed in experimental data.[124,125] The difference in temperature between experimental and simulation may be due to the smaller system and the constraint on the simulation as well as minor deficiencies in the intermolecular interactions used. The DW factor is calculated over a wide range of temperatures for TIP4P ices within the framework of classical and quantum harmonic approximation discussed above.[126] Quantum treatment of DW factor exhibits a fairly different characteristic near 0 K. The classical DW factor, however, approaches the quantum behavior at temperatures higher than 150 K. Thus, a classical MD simulation that includes anharmonic interactions is likely to be adequate in examining the origin and the break in the DW factor.

We have examined time evolution of one proton-disordered ice structure for 30 ns at temperatures of 250, 230, and 200 K. The generated configurations are subjected to the steepest descent energy minimization. The local energy minimum structures thus obtained correspond to the potential energy basin centers (Q-structure) in configuration space. The potential energy of the Q-structures at 250 K is plotted as a function of time in Fig. 27. The potential energy gradually decreases and arrives at a limit. This is interesting because it may correspond to a process that proton-ordering increases. There is almost no exchange of hydrogen-bonded partner at 200 K. The molecular motions are restricted to vibrational ones. When the temperature is raised to 230 K, molecules frequently move from the initial potential basins to adjacent ones, which may include some defects in the hydrogen-bond network but belong to one of potential basin centers. Examination of the MD trajectories at 230 K shows that the system undergoes many transitions to other configurations either satisfying or violating the "ice rule." The system mostly visits near-by potential basins with defects for a short time, and then may return to the initial basin. At 250 K, the system has sufficient kinetic energy to surmount the activation energy barrier that leads to an adjacent basin with no defects within 30 ns.[127] Analysis of the local energy minimum structures shows that water molecules sometimes jump to other lattice sites via intervening mechanically stable structures in which there are a few defects in location and hydrogen bond as shown in Fig. 28. These intervening ice structures belong to Q-structures but are not a sort of the family of the proton-disordered ice forms satisfying the "ice rule": in other words, they contain several water molecules having less than four hydrogen-bonded neighbors, and some molecules are located in regions other than the lattice sites. However, almost all of the molecules occupy their lattice sites. The break in the DW factor indicates the onset temperature above which the jump-like motions dominate.

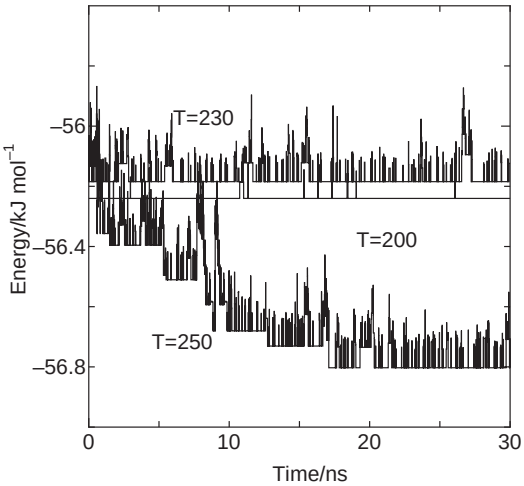

Fig. 27. The time evolution of the potential energy of local minima for 30 ns run at three temperatures (T = 200, 230, and 250 K).

7. Concluding Remarks

We have investigated various interesting properties of water by examining (1) microscopic view of polyamorphism in supercooled water in terms of liquid–liquid transition and potential energy surface, (2) phase behaviors of water and new ice forms in quasi-one- and two-dimensional space, (3) thermodynamic stability of clathrate hydrates beyond classical treatments, and (4) physical origins of some anomalies of ices at atmospheric pressure.

It is demonstrated that there is a significant change in thermodynamic, structural, and dynamic properties of supercooled water around 210 K, suggesting liquid–liquid transition. This transition is induced by changes in the potential energy surface and connectivity of hydrogen-bond network, which seem to be the keys to understanding liquid–liquid transitions.

Tetrahedral coordination is preserved even in extreme confinements, forming novel tubule ice and bilayer crystalline (also amorphous) ice. In quasi-one-dimensional space, both first-order transitions and continuous transformations between liquid-like and ice nanotube are observed depending on the

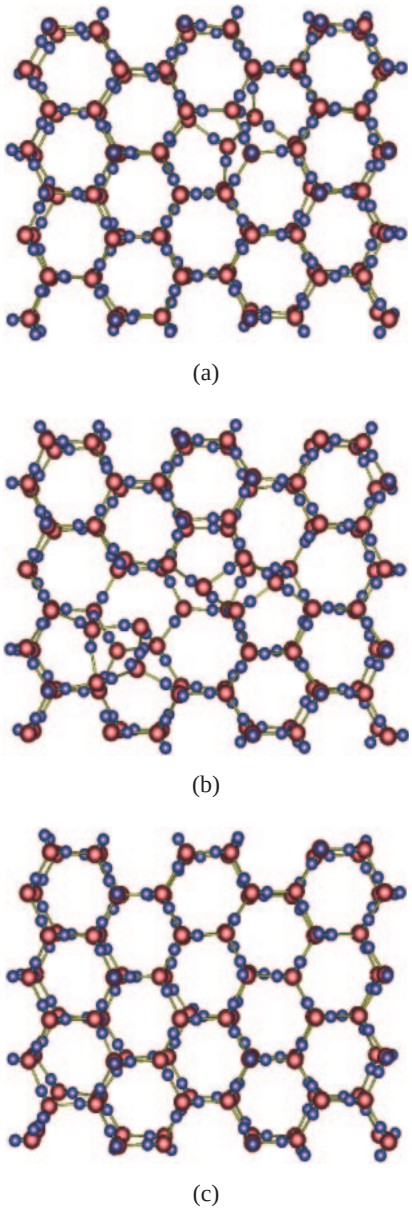

Fig. 28. A snapshot of ice configuration at 250 K. The basic cell has been divided into three sub-boxes, each of which contains 96 molecules.

size of carbon nanotube and also on the applied pressure. This leads to a unique phase behavior which is never observed in three-dimensional space, i.e., a second critical point where a solid–liquid boundary terminates. Such a structure is also found for silicon.[128]

Thermodynamic stability of clathrate hydrates is accurately predicted by considering the host–guest coupling. Treatment of double occupancy is implemented in the theoretical calculation, which allows to evaluate cage occupancy correctly up to fairly high pressures. An unusual temperature dependence of the thermal conductivity of clathrate hydrate is elucidated by a host–guest coupled motions.

The negative thermal expansivity of ice Ih (and ice Ic) in low-temperature regimes is accounted for by the low-frequency intermolecular vibrational modes with negative Grüneisen parameters, which arise from bending motions of three hydrogen-bonded molecules. The appearance of a break in temperature dependence of the Debye–Waller factor in ice Ih is associated with migration of water molecules even in crystalline ice structure, which induces proton-ordering.

A part of this work was supported by Grant-in-Aid from JSPS and Ministry of Education in Japan, Okayama Foundation for Science and Technology, Mitsubishi Foundation, and NAREGI nanoscience project. The authors are grateful to Professors I. Ohmine, X. C. Zeng, G. T. Gao, H. E. Stanley, and co-authors of the papers cited in this Account.

References

1 D. Eisenberg, W. Kauzmann, *The Structure and Properties of Water*, Oxford Univ. Press, London, **1969**.
2 *Water: A Comprehensive Treatise*, ed. by F. Franks, Plenum, New York, **1972–1982**, Vols. 1–7.
3 *Water Science Review*, ed. by F. Franks, Cambridge Univ. Press, London, **1985–1990**, Vols. 1–5.
4 I. Ohmine, H. Tanaka, *Chem. Rev.* **1993**, *93*, 2545.
5 W. L. Jorgensen, J. Chandrasekhar, J. D. Madura, R. W. Impey, M. L. Klein, *J. Chem. Phys.* **1983**, *79*, 926.
6 F. H. Stillinger, A. Rahman, *J. Chem. Phys.* **1974**, *60*, 1545.
7 M. W. Mahoney, W. L. Jorgensen, *J. Chem. Phys.* **2000**, *112*, 8910.
8 S. Nosé, *Mol. Phys.* **1984**, *52*, 255; *J. Chem. Phys.* **1984**, *81*, 511.
9 H. C. Andersen, *J. Chem. Phys.* **1980**, *72*, 2384.
10 D. C. Rapaport, *The Art of Molecular Dynamics Simulation*, Cambridge University Press, Cambridge, **1995**.
11 F. H. Stillinger, T. A. Weber, *Phys. Rev. A* **1982**, *25*, 978; *J. Phys. Chem.* **1983**, *87*, 2833.
12 I. Ohmine, H. Tanaka, P. G. Wolynes, *J. Chem. Phys.* **1988**, *89*, 5852.
13 O. Mishima, L. D. Calvert, E. Whalley, *Nature* **1984**, *310*, 393.
14 O. Mishima, L. D. Calvert, E. Whalley, *Nature* **1985**, *314*, 76.
15 P. H. Poole, F. Sciortino, U. Essmann, H. E. Stanley, *Nature* **1992**, *360*, 324.
16 H. E. Stanley, C. A. Angell, U. Essmann, M. Hemmati, P. H. Poole, F. Sciortino, *Physica A* **1994**, *205*, 122.
17 H. Tanaka, *Nature* **1996**, *380*, 328.
18 H. Tanaka, *J. Chem. Phys.* **1996**, *105*, 5099.
19 F. Sciortino, P. H. Poole, U. Essmann, H. E. Stanley, *Phys. Rev. E* **1997**, *55*, 727.
20 O. Mishima, H. E. Stanley, *Nature* **1998**, *396*, 329.
21 T. Kabeya, Y. Tamai, H. Tanaka, *J. Phys. Chem. B* **1998**, *102*, 899.
22 R. J. Speedy, C. A. Angell, *J. Chem. Phys.* **1976**, *65*, 851.
23 R. J. Speedy, *J. Phys. Chem.* **1992**, *96*, 2322.
24 C. A. Angell, *J. Phys. Chem.* **1993**, *97*, 6339.
25 K. Ito, K. C. T. Moynihan, C. A. Angell, *Nature* **1999**, *398*, 492.
26 R. Bergman, J. Swenson, *Nature* **2000**, *403*, 283.
27 Y. Tamai, H. Tanaka, *Phys. Rev. E* **1999**, *59*, 5647.
28 J. L. Finney, D. T. Bowron, A. K. Soper, T. Loerting, E. Mayer, A. Hallbrucker, *Phys. Rev. Lett.* **2002**, *89*, 205503.
29 S. Klotz, G. Hamel, J. S. Loveday, R. J. Nelmes, M.

Gunthrie, A. K. Soper, *Phys. Rev. Lett.* **2002**, *89*, 285502.
30 J. S. Tse, M. L. Klein, *Phys. Rev. Lett.* **1987**, *58*, 1672.
31 I. Okabe, H. Tanaka, *Phys. Rev. E* **1996**, *53*, 2638.
32 R. Martonak, D. Donadio, M. Parrinello, *Phys. Rev. Lett.* **2004**, *92*, 225702.
33 N. Giovambattista, P. G. Debenedetti, F. Sciortino, H. E. Stanley, *Phys. Rev. E* **2005**, *71*, 061505.
34 J. Slovak, H. Tanaka, *J. Chem. Phys.* **2005**, *122*, 204512.
35 H. Tanaka, *J. Chem. Phys.* **2000**, *113*, 11202.
36 P. H. Poole, F. Sciortino, U. Essmann, H. E. Stanley, *Phys. Rev. E* **1993**, *48*, 3799.
37 S. Sastry, P. G. Debenedetti, F. H. Stillinger, *Nature* **1998**, *393*, 554.
38 P. Jund, R. Jullien, *Phys. Rev. Lett.* **1999**, *83*, 2210.
39 C. J. Roberts, P. G. Debenedetti, F. H. Stillinger, *J. Phys. Chem. B* **1999**, *103*, 10258.
40 A. Hallbrucker, E. Mayer, G. P. Johari, *Philos. Mag. B* **1987**, *60*, 179.
41 D. D. Klug, Y. P. Handa, *J. Phys. Chem.* **1988**, *92*, 3323.
42 R. S. Smith, B. D. Kay, *Nature* **1999**, *398*, 788.
43 H. Tanaka, *Phys. Rev. Lett.* **1998**, *80*, 113.
44 H. E. Stanley, J. Teixeira, *J. Chem. Phys.* **1980**, *73*, 3404.
45 T. Head-Gordon, F. H. Stillinger, *J. Chem. Phys.* **1993**, *98*, 3313.
46 D. Stauffer, *Introduction to Percolation Theory*, Tailor and Francis, London and Philadelphia, **1985**.
47 H. Scher, R. Zallen, *J. Chem. Phys.* **1970**, *53*, 1421.
48 F. H. Stillinger, T. A. Weber, *Science* **1984**, *225*, 983.
49 F. H. Stillinger, *Science* **1995**, *267*, 1935.
50 C. A. Angell, *Science* **1995**, *267*, 1924.
51 A. Scala, F. W. Starr, E. L. Nave, F. Sciortino, H. E. Stanley, *Nature* **2000**, *406*, 166.
52 H. Tanaka, I. Ohmine, *J. Chem. Phys.* **1987**, *87*, 6128; H. Tanaka, I. Ohmine, *J. Chem. Phys.* **1989**, *91*, 6318; I. Ohmine, H. Tanaka, *J. Chem. Phys.* **1990**, *93*, 8138.
53 F. Sciortino, P. Tartaglia, *Phys. Rev. Lett.* **1997**, *78*, 2385.
54 V. F. Petrenko, R. W. Withworth, *Physics of Ice*, Oxford University Press, New York, **2003**.
55 K. Koga, G. T. Gao, H. Tanaka, X. C. Zeng, *Nature* **2001**, *412*, 6849.
56 K. Koga, *J. Chem. Phys.* **2002**, *116*, 10882.
57 Y. Maniwa, H. Kataura, M. Abe, S. Suzuki, Y. Achiba, H. Kira, K. Matsuda, *J. Phys. Soc. Jpn.* **2002**, *71*, 2863.
58 A. I. Kolesnikov, J.-M. Zanotti, C.-K. Loong, P. Thiyagarajan, A. P. Moravsky, R. O. Loutfy, C. J. Burnham, *Phys. Rev. Lett.* **2004**, *93*, 035503.
59 M.-C. Bellissent-Funel, S. H. Chen, J. M. Zanotti, *J. Chem. Phys.* **1996**, *104*, 10023.
60 K. Koga, X. C. Zeng, H. Tanaka, *Phys. Rev. Lett.* **1997**, *79*, 5262.
61 M. Meyer, H. E. Stanley, *J. Phys. Chem. B* **1999**, *103*, 9728.
62 K. Koga, H. Tanaka, X. C. Zeng, *Nature* **2000**, *408*, 564.
63 M. C. Gordillo, J. Marti, *Chem. Phys. Lett.* **2000**, *329*, 341.
64 I. Brovchenko, A. Geiger, A. Oleinikova, *Phys. Chem. Chem. Phys.* **2001**, *3*, 1567.
65 G. Hummer, J. C. Rasaiah, J. P. Noworyta, *Nature* **2001**, *414*, 188.
66 K. Koga, R. D. Parra, H. Tanaka, X. C. Zeng, *J. Chem. Phys.* **2000**, *113*, 5037.
67 B. Bai, R. D. Parra, X. C. Zeng, H. Tanaka, K. Koga, J.-M. Li, *J. Chem. Phys.* **2003**, *118*, 3913.
68 C. J. Tsai, K. D. Jordan, *J. Phys. Chem.* **1993**, *97*, 5208.
69 H. Tanaka, K. Koga, *J. Chem. Phys.* **2005**, *123*, 94706.
70 K. Koga, H. Tanaka, *J. Chem. Phys.* **2005**, *122*, 104711.
71 M. Matsumoto, S. Saito, I. Ohmine, *Nature* **2002**, *416*, 409.
72 L. Pauling, *J. Am. Chem. Soc.* **1935**, *57*, 2680.
73 R. Zallen, *The Physics of Amorphous Solids*, Wiley, New York, **1998**, p. 63.
74 O. Mishima, H. E. Stanley, *Nature* **1998**, *392*, 164.
75 M. O. Thompson, G. J. Galvin, J. W. Mayer, P. S. Peercy, J. M. Poate, D. C. Jacobson, A. G. Cullis, N. G. Chew, *Phys. Rev. Lett.* **1984**, *52*, 2360.
76 C. A. Angell, S. Borick, M. Grabow, *J. Non-Cryst. Solids* **1996**, *207*, 463.
77 M. Togaya, *Phys. Rev. Lett.* **1997**, *79*, 2474.
78 J. N. Glosli, F. H. Ree, *Phys. Rev. Lett.* **1999**, *82*, 4659.
79 Y. Katayama, T. Mizutani, W. Utsumi, O. Shimomura, M. Yamakata, K. Funakoshi, *Nature* **2000**, *403*, 170.
80 F. Franks, *Water: A Comprehensive Treatise*, ed. by F. Franks, Plenum, New York, **1973**, Vol. 2.
81 D. W. Davidson, *Water: A Comprehensive Treatise*, ed. by F. Franks, Plenum, New York, **1973**, Vol. 2.
82 E. D. Sloan, *Clathrate Hydrates of Natural Gases*, 2nd ed., Marcel Dekker, New York, **1998**.
83 J. H. van der Waals, J. C. Platteeuw, *Adv. Chem. Phys.* **1959**, *2*, 1.
84 H. Tanaka, K. Kiyohara, *J. Chem. Phys.* **1993**, *98*, 4098.
85 H. Tanaka, K. Kiyohara, *J. Chem. Phys.* **1993**, *98*, 8110.
86 H. Tanaka, *J. Chem. Phys.* **1994**, *101*, 10833.
87 H. Tanaka, T. Nakatsuka, K. Koga, *J. Chem. Phys.* **2004**, *121*, 5488.
88 J. A. Ripmeester, J. S. Tse, C. I. Ratcliffe, B. M. Powell, *Nature* **1987**, *325*, 135.
89 J. O. Hirschfelder, C. F. Curtiss, R. B. Bird, *Molecular Theory of Gases and Liquids*, Wiley, New York, **1954**.
90 B. Kvamme, H. Tanaka, *J. Phys. Chem.* **1995**, *99*, 7114.
91 D. W. Davidson, Y. P. Handa, C. I. Ratcliffe, J. S. Tse, B. M. Powell, *Nature* **1984**, *311*, 142.
92 W. F. Kuhs, B. Chazallon, P. G. Radaelli, P. Pauer, *J. Inclusion Phenom. Mol. Recognit. Chem.* **1997**, *29*, 65.
93 H. Tanaka, K. Nakanishi, *Mol. Simul.* **1994**, *12*, 317.
94 J. J. Nicolas, K. E. Gubbins, W. B. Streett, D. J. Tildesley, *Mol. Phys.* **1979**, *37*, 1429.
95 R. M. Barrer, A. V. J. Edge, *Proc. R. Soc. London, Ser. A* **1967**, *300*, 1.
96 H. T. Lotz, J. A. Schouten, *J. Chem. Phys.* **1999**, *111*, 10242.
97 A. Y. Manakov, V. I. Voromin, A. V. Kurnosov, A. E. Teplykh, E. G. Larionov, Y. A. Dyadin, *Dokl. Phys. Chem.* **2001**, *378*, 148.
98 A. V. Kurnosov, A. Y. Manakov, V. Y. Komarov, V. I. Voromin, A. E. Teplykh, Y. A. Dyadin, *Dokl. Phys. Chem.* **2001**, *381*, 303.
99 H. Shimizu, S. Hori, T. Kume, S. Sasaki, *Chem. Phys. Lett.* **2003**, *368*, 132.
100 Y. P. Handa, J. G. Cook, *J. Phys. Chem.* **1987**, *91*, 6327.
101 J. S. Tse, M. A. White, *J. Phys. Chem.* **1998**, *92*, 5006.
102 R. Inoue, H. Tanaka, K. Nakanishi, *J. Chem. Phys.* **1996**, *104*, 9569.
103 E. M. Hendriks, B. Edmonds, R. A. S. Moorwood, R. Szezepanks, *Fluid Phase Equilib.* **1996**, *117*, 193.
104 S. Subramanian, R. A. Kini, S. F. Dec, E. D. Sloan, *Chem. Eng. Sci.* **2000**, *55*, 1981.

105 S. Takeya, Y. Kamata, T. Uchida, J. Nagao, T. Ebinuma, H. Narita, A. Hori, T. Hondoh, *Can. J. Phys.* **2003**, *81*, 479.
106 Y. Koyama, H. Tanaka, K. Koga, *J. Chem. Phys.* **2005**, *122*, 074503.
107 M. Parrinello, A. Rahman, *Phys. Rev. Lett.* **1980**, *45*, 1196.
108 G. Dantl, *Zeits. für Phys.* **1962**, *166*, 115.
109 J. G. Collins, G. K. White, *Low Temp. Phys.* **1964**, *4*, 450.
110 G. T. Gao, X. C. Zeng, H. Tanaka, *J. Chem. Phys.* **2000**, *112*, 8534.
111 E. Sanz, C. Vega, J. L. F. Abascal, L. G. MacDowell, *Phys. Rev. Lett.* **2004**, *92*, 255701.
112 Y. Koyama, H. Tanaka, G. T. Gao, X. C. Zeng, *J. Chem. Phys.* **2004**, *121*, 7926.
113 Y. P. Handa, D. D. Klug, E. Walley, *J. Chem. Phys.* **1986**, *84*, 7009.
114 O. Mishima, *J. Chem. Phys.* **1994**, *100*, 5910.
115 L. S. Bartell, *Chem. Rev.* **1986**, *86*, 491.
116 H. Tanaka, I. Okabe, *Chem. Phys. Lett.* **1996**, *259*, 593.
117 H. Tanaka, *J. Chem. Phys.* **1988**, *108*, 4887.
118 H. Kiefte, M. J. Clouter, E. Walley, *J. Chem. Phys.* **1984**, *81*, 1491.
119 R. S. Roberts, C. Andrikidis, R. J. Tanish, G. K. White, *Proceedings of the 10th International Cryogenic Engineering Conference*, ed. by H. Callan, P. Bergland, M. Krusius, Butterworths, Helsinki, **1984**.
120 J. S. Tse, G. M. McKinnon, M. March, *J. Phys. Chem.* **1987**, *91*, 4188.
121 Y. S. Touloukian, R. K. Kirby, R. E. Taylor, J. Y. R. Lee, *Thermophysical Properties of Matter*, Plenum, New York, **1977**, Vol. 13, p. 263.
122 H. Tanaka, Y. Tamai, K. Koga, *J. Phys. Chem. B* **1997**, *101*, 6560.
123 J. S. Tse, *Chem. Phys. Lett.* **1993**, *215*, 383.
124 W. F. Kuhs, M. S. Lehmann, *J. Phys. Chem.* **1983**, *87*, 4312.
125 F. Demmel, W. Doster, W. Petry, A. Schulte, *Eur. Biophys. J.* **1997**, *26*, 327.
126 H. Tanaka, U. Mohanty, *J. Am. Chem. Soc.* **2002**, *124*, 8085.
127 O. Haida, T. Matsuo, H. Suga, S. Seki, *Proc. Jpn. Acad.* **1972**, *48*, 237.
128 B. Bai, X. C. Zeng, H. Tanaka, J. K. Zeng, *Proc. Natl. Acad. Sci. U.S.A.* **2004**, *101*, 2664.

Award recipient

Hideki Tanaka was born in Kagawa prefecture in 1956. He obtained his B.E. (1979), M.E. (1981), and Ph.D. (1984) degrees from Kyoto University. In 1984, he became a research fellow in theoretical division, Institute for Molecular Science. He moved back to Kyoto University as a research associate. He was promoted to a professor of Faculty of Science, Okayama University in 1998. He was a visiting professor in Cornell University during 1992–1993 and in Institute for Molecular Science during 1999–2000. His research interest has been focused on structure and dynamics of water and ice in bulk and confined geometry and on thermodynamic stability of clathrate hydrates.

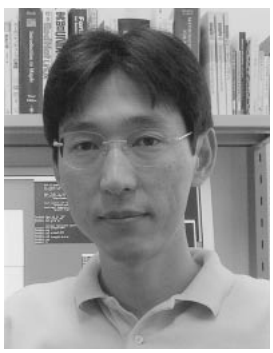

Kenichiro Koga, an associate professor at Okayama University, was born 1968 in Kobe, received his bachelor's degree at Osaka University in 1991, and earned his doctor degree at Kyoto University in 1996. He became a postdoctoral fellow at University of Nebraska in 1996 and was appointed lecturer in 1999 and an associate professor in 2000 at Fukuoka University of Education. He was awarded JSPS postdoctoral fellowship for research abroad, enabling him to be a visiting scientist at Cornell University between 2001 and 2003. His principal research interests are phase equilibria and phase transitions, interfacial phenomena, and molecular theory of liquid and liquid mixtures.